Engineering with Computers
https://doi.org/10.1007/s00366-020-01246-x

ORIGINAL ARTICLE

Dynamic simulation of moderately thick annular system coupled with shape memory alloy and multi-phase nanocomposite face sheets

Haiquan Wang[1] · Hongyan Zhang[1] · Ramin Dousti[2] · Hamed Safarpour[3]

Received: 16 August 2020 / Accepted: 16 December 2020

Abstract
The current research work analyzes dynamics of a sandwich disk which is gently thick. The mentioned sandwich structure has honeycomb core, a couple of middle layers having fibers of shape memory alloy (SMA), and a couple of external layers of multi-scaled hybrid nanocomposite (MHC) considering in-plane force. The core in the shape of honeycomb is manufactured of aluminum due to its high stiffness and less density compared with other materials. Applying energy methods called the principle of Hamilton, we obtained governing motion equations of the mentioned structure and solved them using First-order shear-deformation-theory (FSDT), as well as generalized-differential-quadrature-method (GDQM), respectively. To layers' joint, the compatibility equations have been taken into account. Then, a parametric mathematical manipulation has been conducted to analyze the impacts of fibers of SMA, boundary conditions (BCs), internal loads, honeycomb network angle, ratio of external to internal radiuses, ratio of thickness to length of the honeycomb, weight fraction of CNTs, angle of fibers, ratio of honeycomb to face-sheet thickness on the frequency of the multi-phase sandwich disk. The outcomes derived reveal that for any amount of internal pressure and each BC, the relation of the honeycomb's thickness ratios to MHC layer (h_H/h_t) and sandwich structure's frequency is similar to quadratic function. Further results show that the effects of the fibers' angle on the frequency can be ignored for larger h_H/h_t amounts.

Keywords Honeycomb core · Porosity · Multi-layer disk · Various boundary conditions · MHC · SMA fibers

1 Introduction

Since applicable material and structures' thermomechanical response has been improved by applying the sandwich module structures, in the last decant, scientists discovered a new and perfect method to boost the dynamic and static responses of the low-density beam, plate, disk, and shell [1–7] due to the mentioned fact, structures in honeycomb shape [8, 9] are presented to use in the pertained industries [10, 11]. The sandwich panel's frequency parameters made from Honeycomb Core have been analyzed by Mukhopadhyay et al. [12] using Energy Methods. In that paper, it is reported that core of honeycomb would enhance the free vibration characteristics and ultimately the sandwich panels' stiffness. Ref. [13] has investigated the impacts of a wide range of defects occurring to build honeycomb composite beams and determined the mechanical behavior of those structures in different frequency modes employing Fast Fourier Transform analyzer and finite element (FE) model. Considerable outcomes of this research revealed that the structure's frequency parameters would be reduced by increasing percentage of structure's defect. Frequency characteristics of honeycomb sandwich structures with various cores have been analyzed by Mozafari et al. [14] Employing experimental tests, they obtained the polyurethane foams' mechanical behaviors and evaluated the impact of the first

✉ Haiquan Wang
haiquan202@hotmail.com

Hongyan Zhang
zhanghy@wfu.edu.cn

Ramin Dousti
ramin.dousti.iut@gmail.com

Hamed Safarpour
hamed.safarpour@edu.ikiu.ac.ir

1 Chemistry and Chemical Engineering and Environmental College, Weifang University, Weifang 261061, Shandong, China

2 Department of Civil Engineering, Isfahan University of Technology (IUT), Isfahan, Iran

3 Faculty of Engineering, Department of Mechanics, Imam Khomeini International University, Qazvin, Iran

resonance, the foams' impact and the shape of the state on the core's vibrations. The frequency characteristics of the structure's graded corrugated lattice core along with using an exact solution method to solve the governing motion equations has been evaluated by Ref. [15]. They studied the beam length's impact, thickness of facial leaf and graded parameters on the mentioned structure's frequency. The amplitude of the solar panel's vibrations which is manufactured by smart layers and honeycomb core has been controlled by Amini et al. [16]. Using the theories related to thin plate and employing Hamilton's principle, they obtained the BCs and equations of motion. Eventually, they discovered that elastoelectric impacts are playing prominent roles in the solar panel's frequency parameters. Ref. [17] examined the panels' post-buckling response with graphene particles reinforcements and honeycomb cores. The scientists' achievements show that the thickness of core, weight fraction of GPL, and geometric characters pertained to panel have vital roles on the sandwich panel's post-buckling. Sobhy [18] has analyzed the curved beam's bending characters reinforced with layers of graphene nanoplatelets along with honeycomb core. Employing DQM, they obtained the associated BCs and solved complicated motion equations. Sandwich panels' frequency parameters with honeycomb core employing FE model and experimental research has been conducted by Wang et al. [19]. They eventually revealed that, the face-sheet's thickness ratio, and density of filling foam have essential role in the sandwich panels' frequency with honeycomb core. Frequency investigation of a sandwich beam considering honeycomb hybrid core applying experimental techniques and FE models has been studied by Ref. [20]. Honeycomb sandwich shell's nonlinear frequency parameters has been reported by Zhang et al. [21]. They have solved the structure's governing motion equations with simply BCs through using method of homotopy perturbation. Recently, applying reinforcements of CNTs have attracted the attention of many scientists and researchers. For instance, an FG circular plate's major bending behavior boosted through using CNTs and covered by an elastic foundation has been studied by Keleshteri et al. [22]. They assert that the thick shear deformation models and von Karman are used to present more precise results in their mathematical method. Moreover, for solving governing equations extracted through using energy methods, they applied the Newton–Raphson as well as GDQ approach. Their prominent result is that the CNT's volume fraction along with thickness would play an important role when it comes to the analysis of the circular disk's nonlinear frequency. Nonlinear free and forced an FG disk's frequency response employing the von Kármán model along with thin SDT has been conducted by Ansari and Torabi [23]. They highlighted basically on the enhanced GDQ approach for the solution method of the FG disk's governing equation and presented a structure's large amplitude frequency. Torabi and Ansari [24] have presented that it is vital to develop motion equations of the FG-CNT-reinforced circular plate's large amplitude vibration based on general asymmetric's equations in the existence of elementary thermally stress for reaching precise outcomes. Finally, a huge number of researches presented the stability/sinstability of applicable structure in many articles [25–33].

Based on the highly scrutinized literature investigation, no one would assert there is a study on the sandwich disk's frequency analysis considering a core (honeycomb), including fiber of shape memory alloy (SMA), and a couple of external layers (MHC) under in-plane load. FSDT is employed to stress–strain formulation. Modified Halpin–Tsai model and the Rule of the mixture are involved in providing the efficient the MHC disk's material constant. Using energy methods, the structure's governing equations are extracted. Eventually, the impacts of some physically and geometrically factors of SMA fiber and MHC and in-plane loads on the dynamics of the mentioned structure are reported, in detail. The final results reveal that we would conclude that using the network of honeycomb as the structure's core boosts the structure's dynamics considerably.

2 Mathematical modeling

2.1 The homogenization process of MHC

The homogenization procedure is contained of a couple of basic stages due to the Halpin–Tsai theory [34], combined with a micromechanical model. The primary level is involved with calculating the efficient behaviors of the composite enhanced with CF as below [35]

$$E_{11} = V_F E_{11}^F + V_{\mathrm{NCM}} E^{\mathrm{NCM}}, \tag{1}$$

$$\frac{1}{E_{22}} = \frac{V_F}{E_{22}^F} + \frac{V_{\mathrm{NCM}}}{E^{\mathrm{NCM}}} - V_F V_{\mathrm{NCM}} \times \frac{(\nu^F)^2 \frac{E^{\mathrm{NCM}}}{E_{22}^F} + (\nu^{\mathrm{NCM}})^2 \frac{E_{22}^F}{E^M} - 2\nu^F \nu^{\mathrm{NCM}}}{V_F E_{22}^F + V_{\mathrm{NCM}} E^{\mathrm{NCM}}}, \tag{2}$$

$$\frac{1}{G_{12}} = \frac{V_F}{G_{12}^F} + \frac{V_{\mathrm{NCM}}}{G^{\mathrm{NCM}}}, \tag{3}$$

$$\rho = V_{\mathrm{NCM}} \rho^{\mathrm{NCM}} + V_F \rho^F, \tag{4}$$

$$\nu_{12} = V_{\mathrm{NCM}} \nu^{\mathrm{NCM}} + V_F \nu^F. \tag{5}$$

The nanocomposite matrixes [36–38] and fiber's volume fraction may be as [35]:

$$V_F + V_{\mathrm{NCM}} = 1. \tag{6}$$

The following stage is organized to determine the efficient behaviors of the nano-scaled composite matrix enhanced with CNTs using the developed micromechanics of Halpin–Tsai [39]:

$$E^{\mathrm{NCM}} = E^M\left(\frac{5}{8}\left(\frac{1+2\beta_{dd}V_{\mathrm{CNT}}}{1-\beta_{dd}V_{\mathrm{CNT}}}\right)+\frac{3}{8}\left(\frac{1+2(l^{\mathrm{CNT}}/d^{\mathrm{CNT}})\beta_{dl}V_{\mathrm{CNT}}}{1-\beta_{dl}V_{\mathrm{CNT}}}\right)\right). \tag{7}$$

Here, β_{dl} and β_{dd} may be calculated as the following relations

$$\beta_{dl} = \frac{(E_{11}^{\mathrm{CNT}}/E^M)}{(l^{\mathrm{CNT}}/2t^{\mathrm{CNT}})+(E_{11}^{\mathrm{CNT}}/E^M)} - \frac{(d^{\mathrm{CNT}}/4t^{\mathrm{CNT}})}{(l^{\mathrm{CNT}}/2t^{\mathrm{CNT}})+(E_{11}^{\mathrm{CNT}}/E^M)},$$
$$\beta_{dd} = \frac{(E_{11}^{\mathrm{CNT}}/E^M)}{(d^{\mathrm{CNT}}/2t^{\mathrm{CNT}})+(E_{11}^{\mathrm{CNT}}/E^M)} - \frac{(d^{\mathrm{CNT}}/4t^{\mathrm{CNT}})}{(d^{\mathrm{CNT}}/2\times t^{\mathrm{CNT}})+(E_{11}^{\mathrm{CNT}}/E^M)}. \tag{8}$$

The CNTs' volume fraction would be calculated as follow:

$$V_{\mathrm{CNT}}^{*} = \frac{W_{\mathrm{CNT}}}{W_{\mathrm{CNT}}+\left(\frac{\rho^{\mathrm{CNT}}}{\rho^{M}}\right)(1-W_{\mathrm{CNT}})}. \tag{9}$$

However, a broad range of MHC distribution through orientation of thickness would be written by [40]:

$$\begin{aligned} V_{\mathrm{CNT}} &= 4V_{\mathrm{CNT}}^{*}\frac{\left|\xi_j\right|}{h} \quad \text{FG - X}\\ V_{\mathrm{CNT}} &= 2V_{\mathrm{CNT}}^{*}\left(1-2\frac{\left|\xi_j\right|}{h}\right) \text{FG-O}\\ V_{\mathrm{CNT}} &= V_{\mathrm{CNT}}^{*} \quad \text{FG - UD}\end{aligned} \tag{10}$$

where $\xi_j = \left(\frac{1}{2}+\frac{1}{2N_t}-\frac{j}{N_t}\right)$, $j = 1,2,\ldots,N_t$.

Moreover, the sum of V_{CNT} and V_{M} is equal to one as below (Fig. 1):

$$V_{\mathrm{CNT}} + V_M = 1. \tag{11}$$

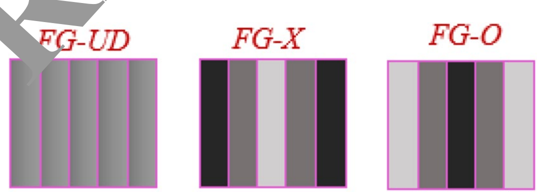

Fig. 1 Distribution of CNT through the thickness of the MHL composite

Eventually, the MHC face sheets' mechanical properties may be written as:

$$\rho^{NCM} = V_{CNT}\rho^{CNT} + V_M\rho^M \tag{12}$$

$$\nu^{\mathrm{NCM}} = \nu^M, \tag{13}$$

$$G^{NCM} = \frac{E^{NCM}}{2\left(1+\nu^{NCM}\right)} \tag{14}$$

In Fig. 2, different types of porosity distribution called, X, U, along with O are given [41–44]. The shear modulus, Young's modulus as well as density, are as follow:

$$\tilde{G}_{12}(z) = \frac{\tilde{E}_{22}}{2(1-\nu(z))} \tag{15a}$$

$$\tilde{E}_{22} = E_{22}\left(1-e_0 s(z)\right), \tag{15b}$$

$$\tilde{E}_{11} = E_{11}\left(1-e_0 s(z)\right), \tag{15c}$$

$$\tilde{\rho}(z) = \left[-e_m s(z)+1\right]\rho(z) + V_{ncm}\rho_{ncm}, \tag{15d}$$

where [45]:

$$s = \begin{cases} s_o & \mathrm{PD-UD}\\ s_o\cos\left(\frac{\pi}{4}+\frac{\pi z}{2h}\right) & \mathrm{PD}-X\\ s_o\cos\left(\frac{\pi z}{h}\right) & \mathrm{PD}-O \end{cases}. \tag{16}$$

Due to the Gaussian Random Field scheme (Figs. 3 and 4), we would have [45]:

$$e_m = \frac{1.121\left[1-\left(1-e_0 s(z)\right)^{\frac{1}{2.3}}\right]}{s(z)}, \tag{17}$$

the porous disk's Poisson's ratio pertaining to the Field of closed-cell Gaussian Random would be computed as [45]:

$$\begin{aligned}\tilde{\nu}_{12} = {} & 0.221\left(1-\frac{\tilde{\rho}(z)}{\rho}\right)\\ & + \nu_{12}\left[1+0.342\left(1-\frac{\tilde{\rho}(z)}{\rho}\right)^2 - 1.21\left(1-\frac{\tilde{\rho}(z)}{\rho}\right)\right],\end{aligned} \tag{18a}$$

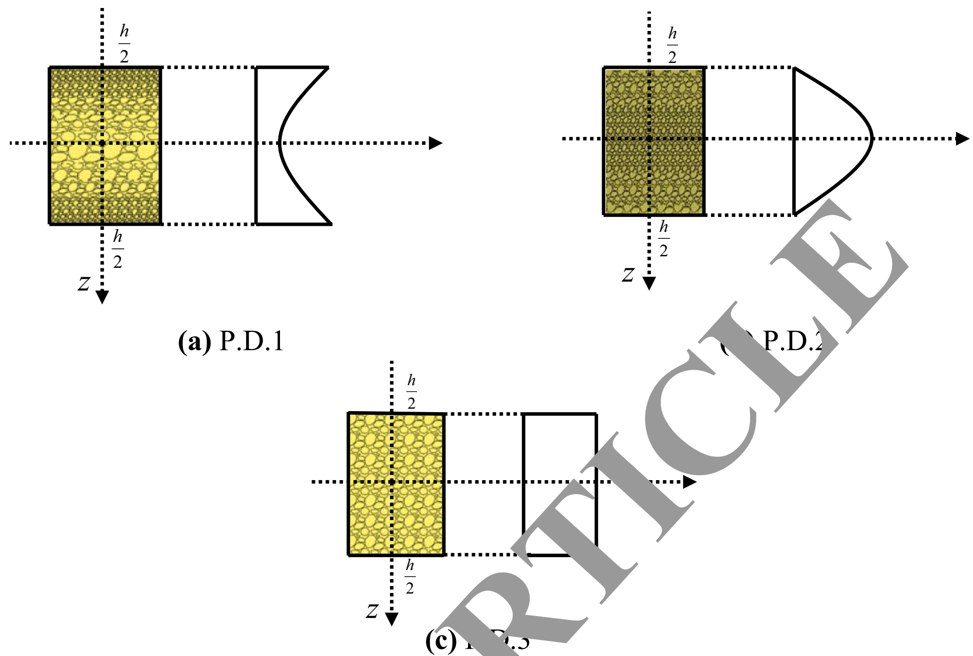

Fig. 2 Patterns of porosity distribution through the thickness of MHC [46]

$$\tilde{v}_{21} = \tilde{v}_{12}\frac{\tilde{E}_{11}}{\tilde{E}_{22}}. \tag{18b}$$

Moreover, when the porosity distributions' various types with the disk's total masses are the same, the amount of the S_0 may be obtained as [45]:

$$s_0 = \frac{1}{e_0}\left[1 - \left(\frac{\frac{1}{h}\int_{-\frac{h}{2}}^{\frac{h}{2}} \frac{\tilde{\rho}(z)}{\rho}\mathrm{d}z + 0.121}{1.121}\right)^{2.3}\right] \tag{19}$$

3 Honeycomb core modeling

The hexagonal cell configuration is demonstrated in Fig. 3. Due to the Gibson theory, we would have [47]:

$$E_{11}^* = \frac{\sigma_1}{\varepsilon_1} = E_S\left(\frac{t}{l}\right)^3 \frac{\cos\left(\theta_h\right)}{\left(h/l + \sin\left(\theta_h\right)\right)\sin^2\left(\theta_h\right)} \frac{1}{1 + (t/l)^2\cot^2\left(\theta_h\right)} \tag{20-a}$$

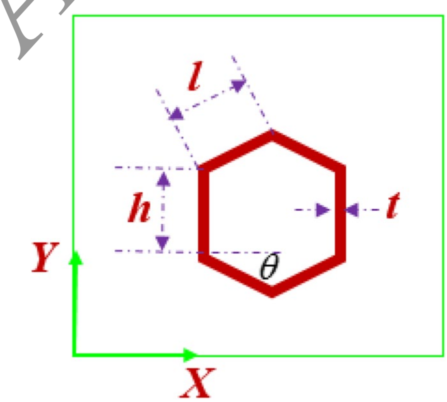

Fig. 3 The hexagonal cell geometry

$$E_{22}^* = \frac{\sigma_2}{\varepsilon_2} = E_S\left(\frac{t}{l}\right)^3 \frac{\left(h/l + \sin\left(\theta_h\right)\right)}{\cos^3\left(\theta_h\right)} \frac{1}{1 + (t/l)^2\cot^2\left(\theta_h\right)} \tag{20-b}$$

$$v_{12}^* = -\frac{\varepsilon_2}{\varepsilon_1} = \frac{\cos^2\left(\theta_h\right)}{\left(h/l + \sin\left(\theta_h\right)\right)\sin\left(\theta_h\right)} \frac{1 - (t/l)^2}{1 + \cot^2\left(\theta_h\right)(t/l)^2} \tag{20-c}$$

$$v_{21}^* = -\frac{\varepsilon_1}{\varepsilon_2} = \frac{\left(h/l + \sin\left(\theta_h\right)\right)\sin\left(\theta_h\right)}{\cos^2\left(\theta_h\right)} \frac{-(t/l)^2 + 1}{1 + \left((h/l)\sec^2\left(\theta_h\right) + \tan^2\left(\theta_h\right)\right)(t/l)^2} \tag{20-d}$$

$$G^*_{12} = E_S\left(\frac{t}{l}\right)^3 \frac{\left(h/l + \sin\left(\theta_h\right)\right)}{(h/l)^2 \cos\left(\theta_h\right)} \frac{1}{R} \tag{20-e}$$

$$R = \left(2\frac{h}{l} + 1 + \left(\frac{t}{l}\right)^2 \frac{h/l + \sin\left(\theta_h\right)}{(h/l)^2}\left[\left(\sin\left(\theta_h\right) + h/l\right)\tan^2\left(\theta_h\right) + \sin\left(\theta_h\right)\right]\right) \tag{20-f}$$

$$\frac{\rho^*}{\rho_S} = \frac{\left(\frac{t}{l}\right)\left(\frac{h}{l} + 2\right)}{2\cos\left(\theta_h\right)\left(\frac{h}{l} + \sin\left(\theta_h\right)\right)} \tag{20-g}$$

4 SMA characteristics in the composite's matrix

The SMA properties are reported by Ref. [48] the present research, supposed that the fibers of SMA have been distributed uniformly. The composite disk's elastic parameters with fibers of SMA may be derived by [48]:

$$\tilde{E}^{sma}_{11} = V_m E^m_{11} + V_S E_S \tag{21a}$$

$$\tilde{E}^{sma}_{22} = \frac{E_S E^m_{22}}{V_m E^m_{22} + V_m E_m} \tag{21b}$$

$$\tilde{G}^{sma}_{12} = \frac{G_S G^m_{12}}{G_S G^m_{12} + G_S V_m} \tag{21c}$$

$$\tilde{G}^{sma}_{23} = G^m_{23} V_m + G_S V_S \tag{21d}$$

$$\tilde{G}^{sma}_{13} = \tilde{G}^{sma}_{23} \tag{21e}$$

$$\tilde{v}^{sma}_{12} = V_m v^m_{12} + V_S v_S \tag{21f}$$

$$\tilde{\rho}^{sma} = V_m \rho_m + V_S \rho_S \tag{21g}$$

5 The disk's displacement fields

According to the shear stress theories [49–56], and due to the FSDT, the fields of displacement would be expressed by the following equations relations [57]:

$$\begin{aligned} \alpha^\eta &= \alpha^\eta_0 + z\xi^\eta_R \\ \beta^\eta &= \beta^\eta_0 + z\xi^\eta_\theta \\ \chi^\eta &= \chi^\eta_0 \end{aligned} \tag{22}$$

The above equation η explains the bottom, top, along with core layers.

6 Stress–Strain honeycomb core's relations

Due to the FSDT, the stress–strain relation may be given as [57–63]:

$$\begin{bmatrix} \sigma_{RR} \\ \sigma_{\theta\theta} \\ \sigma_{R\theta} \\ \sigma_{Rz} \\ \sigma_{\theta z} \end{bmatrix}^c = \begin{bmatrix} Q_{11} & Q_{12} & 0 & 0 & 0 \\ Q_{12} & Q_{22} & 0 & 0 & 0 \\ 0 & 0 & Q_{66} & 0 & 0 \\ 0 & 0 & 0 & Q_{55} & 0 \\ 0 & 0 & 0 & 0 & Q_{44} \end{bmatrix}^c \begin{bmatrix} \varepsilon_{RR} \\ \varepsilon_{\theta\theta} \\ \gamma_{R\theta} \\ \gamma_{Rz} \\ \gamma_{\theta z} \end{bmatrix}^c$$

$$Q^c_{11} = \frac{E^*_{11}}{1 - v^*_{12} v^*_{21}},\quad Q^c_{22} = \frac{E^*_{22}}{1 - v^*_{12} v^*_{21}},\quad Q^c_{12} = \frac{v^*_{21} E^*_{22}}{1 - v^*_{12} v^*_{21}},$$
$$Q^c_{44} = G^*_{12},\quad Q^c_{55} = G^*_{13},\quad Q^c_{66} = G^*_{23},\quad G^*_{13} = G^*_{23} = G^*_{12} \tag{23}$$

So, the strain elements may be defined as [64]:

$$\begin{Bmatrix} \varepsilon_{RR} \\ \varepsilon_{\theta\theta} \\ \gamma_{R\theta} \\ \gamma_{Rz} \\ \gamma_{\theta z} \end{Bmatrix}^\psi = \begin{Bmatrix} \varepsilon^0_{RR} \\ \varepsilon^0_{\theta\theta} \\ \gamma^0_{R\theta} \\ \gamma^0_{Rz} \\ \gamma^0_{\theta z} \end{Bmatrix}^\psi + z \begin{Bmatrix} \kappa_{RR} \\ \kappa_{\theta\theta} \\ \kappa_{R\theta} \\ \kappa_{Rz} \\ \kappa_{\theta z} \end{Bmatrix}^\psi \tag{24}$$

Equation (24) would be rewritten as

$$\begin{Bmatrix} \varepsilon^0_{RR} \\ \varepsilon^0_{\theta\theta} \\ \gamma^0_{R\theta} \\ \gamma^0_{Rz} \\ \gamma^0_{\theta z} \end{Bmatrix}^c = \begin{Bmatrix} \frac{\partial\alpha_0}{\partial R} \\ \frac{\alpha_0}{R} + \frac{\partial\beta_0}{R\partial\theta} \\ \frac{\partial\alpha_0}{R\partial\theta} + \frac{\partial\beta_0}{\partial R} - \frac{\beta_0}{R} \\ \xi_R + \frac{\partial\chi}{\partial R} \\ \xi_\theta + \frac{\partial\chi}{R\partial\theta} \end{Bmatrix}^c, \quad \begin{Bmatrix} \kappa_{RR} \\ \kappa_{\theta\theta} \\ \kappa_{R\theta} \\ \kappa_{Rz} \\ \kappa_{\theta z} \end{Bmatrix}^c = \begin{Bmatrix} \frac{\partial\xi_R}{\partial R} \\ \frac{\xi_R}{R} + \frac{\partial\xi_\theta}{R\partial\theta} \\ \frac{\partial\xi_R}{R\partial\theta} + \frac{\partial\xi_\theta}{\partial R} - \frac{\xi_\theta}{R} \\ 0 \\ 0 \end{Bmatrix}^c \tag{25}$$

MHC angle-ply laminated disk's Stress–strain equations [65–69] and SMA layer would be given as below [57]:

$$\begin{bmatrix} \sigma_{RR} \\ \sigma_{\theta\theta} \\ \sigma_{R\theta} \\ \sigma_{Rz} \\ \sigma_{\theta z} \end{bmatrix}^\psi = \begin{bmatrix} \hat{Q}_{11} & \hat{Q}_{12} & 0 & 0 & \hat{Q}_{16} \\ \hat{Q}_{21} & \hat{Q}_{22} & 0 & 0 & \hat{Q}_{26} \\ 0 & 0 & \hat{Q}_{44} & \hat{Q}_{45} & 0 \\ 0 & 0 & \hat{Q}_{45} & \hat{Q}_{55} & 0 \\ \hat{Q}_{16} & \hat{Q}_{26} & 0 & 0 & \hat{Q}_{66} \end{bmatrix}^\psi \begin{bmatrix} \varepsilon_{RR} \\ \varepsilon_{\theta\theta} \\ \gamma_{R\theta} \\ \gamma_{Rz} \\ \gamma_{\theta z} \end{bmatrix}^\psi \tag{26}$$

In the aforementioned relation, ψ explains the bottom and top layers of the structure.

Here

$$\hat{Q}_{11}^{\psi} = \sin^4\theta_f \tilde{Q}_{22}^{\psi} + \cos^4\theta_f \tilde{Q}_{11}^{\psi} + 2\sin^2\theta_f \cos^2\theta_f \left(\tilde{Q}_{12}^{\psi} + 2\tilde{Q}_{66}^{\psi}\right) \tag{27a}$$

$$\hat{Q}_{12}^{\psi} = +\left(\sin^4\theta_f + \cos^4\theta_f\right)\tilde{Q}_{12}^{\psi} + \sin^2\theta_f \cos^2\theta_f \left(\tilde{Q}_{11}^{\psi} + \tilde{Q}_{22}^{\psi} - 4\tilde{Q}_{66}^{\psi}\right) \tag{27b}$$

$$\begin{Bmatrix} \varepsilon_{RR}^{0} \\ \varepsilon_{\theta\theta}^{0} \\ \gamma_{R\theta}^{0} \\ \gamma_{Rz}^{0} \\ \gamma_{\theta z}^{0} \end{Bmatrix}^{\psi} = \begin{Bmatrix} \frac{\partial \alpha_0}{\partial R} \\ \frac{\alpha_0}{R} + \frac{\partial \beta_0}{R\partial\theta} \\ \frac{\partial \alpha_0}{R\partial\theta} + \frac{\partial \beta_0}{\partial R} - \frac{\beta_0}{R} \\ \xi_R + \frac{\partial \chi}{\partial R} \\ \xi_\theta + \frac{\partial \chi}{R\partial\theta} \end{Bmatrix}^{\psi}, \begin{Bmatrix} \kappa_{RR} \\ \kappa_{\theta\theta} \\ \kappa_{R\theta} \\ \kappa_{Rz} \\ \kappa_{\theta z} \end{Bmatrix}^{\psi} = \begin{Bmatrix} \frac{\partial \xi_R}{\partial R} \\ \frac{\xi_R}{R} + \frac{\partial \xi_\theta}{R\partial\theta} \\ \frac{\partial \xi_R}{R\partial\theta} + \frac{\partial \xi_\theta}{\partial R} - \frac{\xi_\theta}{R} \\ 0 \\ 0 \end{Bmatrix}^{\psi} \tag{29}$$

$$\hat{Q}_{16}^{\psi} = \cos\theta_f \sin^3\theta_f \left(\tilde{Q}_{66}^{\psi} + 2\tilde{Q}_{12}^{\psi} - 2\tilde{Q}_{22}^{\psi}\right) + \cos^3\theta_f \sin\theta_f \left(2\tilde{Q}_{11}^{\psi} - 2\tilde{Q}_{12}^{\psi} - \tilde{Q}_{66}^{\psi}\right) \tag{27c}$$

$$\hat{Q}_{22}^{\psi} = 2\sin^2\theta_f \cos^2\theta_f \tilde{Q}_{12}^{\psi} + \sin^4\theta_f \tilde{Q}_{11}^{\psi} + \cos^4\theta_f \tilde{Q}_{22}^{\psi} + 2\sin^2\theta_f \cos^2\theta_f \left(\tilde{Q}_{12}^{\psi} + 2\tilde{Q}_{66}^{\psi}\right) \tag{27d}$$

$$\hat{Q}_{26}^{\psi} = \cos^3\theta_f \sin\theta_f \left(2\tilde{Q}_{12}^{\psi} - 2\tilde{Q}_{22}^{\psi} + \tilde{Q}_{66}^{\psi}\right) + \cos\theta_f \sin^3\theta_f \left(2\tilde{Q}_{11}^{\psi} - 2\tilde{Q}_{12}^{\psi} - \tilde{Q}_{66}^{\psi}\right) \tag{27e}$$

$$\hat{Q}_{44}^{\psi} = \sin^2\theta_f \tilde{Q}_{55}^{\psi} + \cos^2\theta_f \tilde{Q}_{44}^{\psi} \tag{27f}$$

$$\hat{Q}_{45}^{\psi} = \cos\theta_f \sin\theta_f \left(-\tilde{Q}_{44}^{\psi} + \tilde{Q}_{55}^{\psi}\right) \tag{27g}$$

$$\hat{Q}_{55}^{\psi} = \cos^2\theta_f \tilde{Q}_{55}^{\psi} + \sin^2\theta_f \tilde{Q}_{44}^{\psi} \tag{27h}$$

$$\hat{Q}_{66}^{\psi} = \tilde{Q}_{66}^{\psi}\left(\cos^2\theta_f - \sin^2\theta_f\right)^2 + 4\sin^2\theta_f \cos^2\theta_f \left(\tilde{Q}_{11}^{\psi} + \tilde{Q}_{22}^{\psi} - 2\tilde{Q}_{12}^{\psi}\right) \tag{27i}$$

The terms involved in Eq. (27a–27i) would be obtained as [70–74]:

$$\tilde{Q}_{11}^{\psi} = \frac{\tilde{E}_{11}^{\zeta}}{1 - \tilde{\nu}_{12}\tilde{\nu}_{21}}, \ \tilde{Q}_{12}^{\psi} = \frac{\tilde{\nu}_{12}^{\zeta}\tilde{E}_{22}^{\zeta}}{1 - \tilde{\nu}_{12}^{\zeta}\tilde{\nu}_{21}^{\zeta}}, \ \tilde{Q}_{22}^{\psi} = \frac{\tilde{E}_{22}^{\zeta}}{1 - \tilde{\nu}_{12}^{\zeta}\tilde{\nu}_{21}^{\zeta}}, \ \tilde{Q}_{44}^{\psi} = \tilde{G}_{12}^{\zeta}, \ \tilde{Q}_{55}^{\psi} = \tilde{G}_{23}^{\zeta}, \ \tilde{Q}_{66}^{\psi} = \tilde{G}_{13}^{\zeta}.$$

The aforementioned relations define ζ as the layer of MHLC and SMA. Also, the strain elements could be given as [75, 76]:

$$\begin{Bmatrix} \varepsilon_{RR} \\ \varepsilon_{\theta\theta} \\ \gamma_{R\theta} \\ \gamma_{Rz} \\ \gamma_{\theta z} \end{Bmatrix}^{\psi} = \begin{Bmatrix} \varepsilon_{RR}^{0} \\ \varepsilon_{\theta\theta}^{0} \\ \gamma_{R\theta}^{0} \\ \gamma_{Rz}^{0} \\ \gamma_{\theta z}^{0} \end{Bmatrix}^{\psi} + z\begin{Bmatrix} \kappa_{RR} \\ \kappa_{\theta\theta} \\ \kappa_{R\theta} \\ \kappa_{Rz} \\ \kappa_{\theta z} \end{Bmatrix}^{\psi} \tag{28}$$

Equation (28) can be rewritten as

7 Compatibility equations

The conditions of compatibility supposing excellent bonding between the layers of composite and the core that would be expressed as below:

$$\alpha^{c}(z_c = -h_c/2) = \alpha^{SMAb}(z_{SMAb} = h_{SMAb}/2), \tag{30a}$$

$$\beta^{c}(z_c = -h_c/2) = \beta^{SMAb}(z_{SMAb} = h_{SMAb}/2), \tag{30b}$$

$$\chi^{c}(z_c = -h_c/2) = \chi^{SMAb}(z_{SMAb} = h_{SMAb}/2), \tag{30c}$$

$$\alpha^{c}(z_c = h_c/2) = \alpha^{SMAt}(z_{SMAt} = -h_{SMAt}/2), \tag{30d}$$

$$\beta^{c}(z_c = h_c/2) = \beta^{SMAt}(z_{SMAt} = -h_{SMAt}/2), \tag{30e}$$

$$\chi^{c}(z_c = h_c/2) = \chi^{SMAt}(z_{SMAt} = -h_{SMAt}/2), \tag{30f}$$

$$\alpha^{MHCt}(z_{MHCt} = -h_{cMHCt}/2) = \alpha^{SMAt}(z_{SMAt} = h_{SMAt}/2), \tag{30g}$$

$$\beta^{MHCt}(z_{MHCt} = -h_{MHCt}/2) = \beta^{SMAt}(z_{SMAt} = h_{SMAt}/2), \quad (30h)$$

$$\chi^{MHCt}(z_{MHCt} = -h_{MHCt}/2) = \chi^{SMAt}(z_{SMAt} = h_{SMAt}/2), \quad (30i)$$

$$\alpha^{MHCb}(z_{MHCb} = h_{MHCb}/2) = \alpha^{SMAb}(z_{SMAb} = -h_{SMAb}/2), \quad (30j)$$

$$\chi^{MHCb}(z_{MHCb} = h_{MHCb}/2) = \beta^{SMAb}(z_{SMAb} = -h_{SMAb}/2), \quad (30k)$$

$$\chi^{MHCb}(z_{MHCb} = h_{MHCb}/2) = \chi^{SMAb}(z_{SMAb} = -h_{SMAb}/2). \quad (30l)$$

8 Developed principle of Hamilton

Due to the energy method, there are equations between motion equations and BCs defined as [77, 78]:

$$\int_{t_1}^{t_2} (\delta T^* - \delta U^* + \delta W^*)^\eta \, dt = 0 \quad (31)$$

The related rotating system's kinetic energy may be calculated as [79–84]:

$$T^{*\eta} = \int_V \frac{1}{2}\rho^\eta \left[\left(\frac{\partial \alpha}{\partial t}\right)^2 + \left(\frac{\partial \beta}{\partial t}\right)^2 + \left(\frac{\partial \chi}{\partial t}\right)^2 \right]^\eta dV \quad (32)$$

$$\delta T^{*\eta} = \int_V \rho^\eta \left(\frac{\partial U}{\partial t}\frac{\partial \delta U}{\partial t} + \frac{\partial V}{\partial t}\frac{\partial \delta V}{\partial t} + \frac{\partial W}{\partial t}\frac{\partial \delta W}{\partial t} \right)^\eta dV :$$

$$\delta T^{*\eta} = \int_{R_1}^{R_2}\int_0^\theta \begin{bmatrix} \left\{ -I_0 \frac{\partial^2 \alpha_0}{\partial t^2} - I_1 \frac{\partial^2 \xi_R}{\partial t^2} \right\}\delta\alpha + \left\{ -I_1 \frac{\partial^2 \alpha_0}{\partial t^2} - I_2 \frac{\partial^2 \xi_R}{\partial t^2} \right\}\delta\xi_R \\ + \left\{ c_1 I_3 \frac{\partial^2 \alpha_0}{\partial t^2} + c_1 I_4 \frac{\partial^2 \xi_R}{\partial t^2} \right\}\delta\xi_R + \left\{ -I_0 \frac{\partial^2 \beta_0}{\partial t^2} - I_1 \frac{\partial^2 \xi_\theta}{\partial t^2} \right\}\delta\beta \\ + \left\{ -I_1 \frac{\partial^2 \beta_0}{\partial t^2} - I_2 \frac{\partial^2 \xi_\theta}{\partial t^2} \right\}\delta\xi_\theta + \left\{ -I_0 \frac{\partial^2 \chi_0}{\partial t^2} \right\}\delta\chi \end{bmatrix}^\eta R dR d\theta \quad (33)$$

where:

$$\{I_i\} = \int_{-h/2}^{h/2} \rho^\eta(z)\{z^i\} dZ, \; i = 0 : 4 \quad (34)$$

However, the presented composite structure's strain energy [85–88] could be determined as:

$$\delta U^{*\eta} = \frac{1}{2}\iiint_V \sigma_{ij}^\eta \delta\varepsilon_{ij}^\eta dV$$

$$= \int_A \begin{bmatrix} \left(P_{RR}\frac{\partial \delta\alpha_0}{\partial R} + Q_{RR}\frac{\partial \delta\alpha_1}{\partial R} \right) \\ + \left(P_{\theta\theta}\frac{\partial \delta\beta_0}{R\partial\theta} + Q_{\theta\theta}\frac{\partial \delta\beta_1}{R\partial\theta} + P_{\theta\theta}\frac{\delta\alpha_0}{R} + Q_{\theta\theta}\frac{\delta\alpha_1}{R} \right) \\ + \begin{pmatrix} P_{R\theta}\frac{\partial \delta\beta_0}{\partial R} + Q_{R\theta}\frac{\partial \delta\beta_1}{\partial R} + P_{R\theta}\frac{\partial \delta\alpha_0}{R\partial\theta} + Q_{R\theta}\frac{\partial \delta\alpha_1}{R\partial\theta} \\ -P_{R\theta}\frac{\delta\beta_0}{R} - Q_{R\theta}\frac{\delta\beta_1}{R} \end{pmatrix} \\ + \left((P_{Rz})\left(\delta\alpha_1 + \frac{\partial \delta\chi_0}{\partial R} \right) \right) + \left((P_{\theta z})\left(\delta\beta_1 + \frac{\partial \delta\chi_0}{R\partial\theta} \right) \right) \end{bmatrix}^\eta dA \quad (35)$$

which [89]:

$$\{P_{RR}, Q_{RR}\}^\eta = \int_z \{\sigma_{RR}, z\sigma_{RR}\}^\eta dz;$$
$$\{P_{\theta\theta}, Q_{\theta\theta}\}^\eta = \int_z \{\sigma_{\theta\theta}, z\sigma_{\theta\theta}\}^\eta dz;$$
$$\{P_{Rz}, Q_{Rz}, T_{Rz}\}^\eta = \int_z \{\sigma_{Rz}, z\sigma_{Rz}, z^2\sigma_{Rz}\}^\eta dz;. \quad (36)$$
$$\{P_{R\theta}, Q_{R\theta}, T_{R\theta}\}^\eta = \int_z \{\sigma_{R\theta}, z\sigma_{R\theta}, z^2\sigma_{R\theta}\}^\eta dz;$$
$$\{P_{\theta z}, Q_{\theta z}, T_{\theta z}\}^\eta = \int_z \{\sigma_{\theta z}, z\sigma_{\theta z}, z^2\sigma_{\theta z}\}^\eta dz.$$

Additionally, the variation of the work done [82, 90–93] by mechanical force (internal load) can be obtained as

$$W^{*\eta} = -\int_A P^A \left(\frac{\partial^2 \chi_0^\eta}{\partial R^2} \right) dA \quad (37)$$

Ultimately, corresponding BCs and governing equations would be extracted by inserting Eqs. (37), (35), and (33) in principle of Hamilton (Eq. (31)) which may be written as:

$\delta\alpha_0^\eta$:

$$\frac{\partial}{\partial R}P_{RR}^\eta - \frac{P_{\theta\theta}^\eta - P_{RR}^\eta}{R} + \frac{\partial}{R\partial\theta}P_{R\theta}^\eta = I_0^\eta\frac{\partial^2\alpha_0^\eta}{\partial t^2} + I_1^\eta\frac{\partial^2\alpha_1^\eta}{\partial t^2} \tag{38a}$$

$\delta\beta_0^\eta$:

$$\frac{\partial}{R\partial\theta}P_{\theta\theta}^\eta + \frac{2P_{R\theta}^\eta}{R} + \frac{\partial}{\partial R}P_{R\theta}^\eta = I_0^\eta\frac{\partial^2\beta_0^\eta}{\partial t^2} + I_1^\eta\frac{\partial^2\beta_1^\eta}{\partial t^2} \tag{38b}$$

$\delta\chi_0^\eta$:

$$2\frac{\partial}{\partial R}\left(P_{Rz}\right)^\eta + 2\frac{\partial}{R\partial\theta}\left(P_{\theta z}\right)^\eta - P^A\frac{\partial^2\chi_0}{\partial R^2} = \left(I_0\frac{\partial^2\chi_0}{\partial t^2}\right)^\eta \tag{38c}$$

$\delta\xi_R^\eta$:

$$\frac{\partial Q_{RR}}{\partial R} - \frac{Q_{\theta\theta}}{R} + \frac{1}{R}\frac{\partial Q_{R\theta}}{\partial\theta} - \left(P_{RZ}\right) = I_1\frac{\partial^2\alpha_0}{\partial t^2} + I_2\frac{\partial^2\xi_R}{\partial t^2} \tag{38d}$$

$\delta\xi_\theta$:

$$\frac{\partial}{R\partial\theta}Q_{\theta\theta} + \frac{2}{R}Q_{R\theta} + \frac{\partial}{\partial R}Q_{R\theta} - Q_{\theta z} = I_1^\eta\frac{\partial^2\beta_0}{\partial t^2} + I_2^\eta\frac{\partial^2\xi_\theta}{\partial t^2} \tag{38e}$$

Furthermore, general pertained BCs would be written as:

$$\delta\alpha^\eta = 0 \text{ or } \mathrm{P}_{RR}^\eta\hat{n}_R + \frac{\mathrm{P}_{R\theta}^\eta}{R}\hat{n}_\theta = 0 \tag{39a}$$

$$\delta\beta^\eta = 0 \text{ or } \mathrm{P}_{R\theta}^\eta\hat{n}_R + \frac{\mathrm{P}_{\theta\theta}^\eta}{R}\hat{n}_\theta = 0 \tag{39b}$$

$$\delta\chi^\eta = 0 \text{ or } \left[2\left(P_{RZ}\right)\right]^\eta\hat{n}_R + \left[\frac{2}{R}\left(P_{\theta Z}\right)\right]^\eta\hat{n}_\theta = 0 \tag{39c}$$

$$\delta\chi_R^\eta = 0 \text{ or } \left[\mathrm{Q}_{RR}\right]^\eta\hat{n}_R + \left[\frac{\mathrm{Q}_{R\theta}}{R}\right]^\eta\hat{n}_\theta = 0 \tag{39d}$$

$$\delta\chi_\theta^\eta = 0 \text{ or } \left[\mathrm{Q}_{R\theta}\right]^\eta\hat{n}_R + \left[\frac{\mathrm{Q}_{\theta\theta}}{R}\right]\hat{n}_\theta = 0 \tag{39e}$$

By inserting Eq. (36) into Eqs. (38a–e), the governing equations of the MHLCD are obtained as

$$\begin{aligned}\delta\alpha_0^\eta :\ & \frac{\partial}{\partial R}\left(\left\{\mathbb{R}_{11}\frac{\partial\alpha_0^\eta}{\partial R} + \mathbb{Z}_{11}\frac{\partial\xi_R^\eta}{\partial R}\right\} + \left\{\frac{\mathbb{R}_{12}}{R}\alpha_0^\eta + \frac{\mathbb{Z}_{12}}{R}\xi_R^\eta + \frac{\mathbb{R}_{12}}{R}\frac{\partial\beta_0^\eta}{\partial\theta} + \frac{\mathbb{Z}_{12}}{R}\frac{\partial\xi_\theta^\eta}{\partial\theta}\right\}\right)\\ & + \frac{1}{R}\frac{\partial}{\partial\theta}\left(\frac{\mathbb{R}_{66}}{R}\frac{\partial\alpha_0^\eta}{\partial\theta} + \frac{\mathbb{Z}_{66}}{R}\frac{\partial\xi_R^\eta}{\partial\theta} + \mathbb{R}_{66}\frac{\partial\beta_0^\eta}{\partial R} + \mathbb{Z}_{66}\frac{\partial\xi_\theta^\eta}{\partial R} - \frac{\mathbb{R}_{66}}{R}\beta_0^\eta - \frac{\mathbb{Z}_{66}}{R}\xi_\theta^\eta\right)\\ & - \frac{1}{R}\left(\left\{\mathbb{R}_{12}\frac{\partial\alpha_0^\eta}{\partial R} + \mathbb{Z}_{12}\frac{\partial\xi_R}{\partial R}\right\} + \left\{\frac{\mathbb{R}_{22}}{R}\alpha_0^\eta + \frac{\mathbb{Z}_{22}}{R}\xi_R^\eta + \frac{\mathbb{R}_{22}}{R}\frac{\partial\beta_0^\eta}{\partial\theta} + \frac{\mathbb{Z}_{22}}{R}\frac{\partial\xi_\theta^0}{\partial\theta}\right\}\right)\\ & = I_0^\eta\frac{\partial^2\alpha_0^\eta}{\partial t^2} + I_1^\eta\frac{\partial^2\alpha_1^\eta}{\partial t^2}\end{aligned} \tag{40a}$$

$$\begin{aligned}\delta\beta_0^\eta :\ & \frac{1}{R}\frac{\partial}{\partial\theta}\left(\left\{\mathbb{R}_{12}\frac{\partial\alpha_0^\eta}{\partial R} + \mathbb{Z}_{12}\frac{\partial\xi_R^\eta}{\partial R}\right\} + \left\{\frac{\mathbb{R}_{22}}{R}\alpha_0^\eta + \frac{\mathbb{Z}_{22}}{R}\xi_R^\eta + \frac{\mathbb{R}_{22}}{R}\frac{\partial\beta_0^\eta}{\partial\theta} + \frac{\mathbb{Z}_{22}}{R}\frac{\partial\xi_\theta^\eta}{\partial\theta}\right\}\right)\\ & + \frac{\partial}{\partial\theta}\left(\frac{\mathbb{R}_{66}}{R}\frac{\partial\alpha_0^\eta}{\partial\theta} + \frac{\mathbb{Z}_{66}}{R}\frac{\partial\xi_R^\eta}{\partial\theta} + \mathbb{R}_{66}\frac{\partial\beta_0^\eta}{\partial R} + \mathbb{Z}_{66}\frac{\partial\xi_\theta^\eta}{\partial R} - \frac{\mathbb{R}_{66}}{R}\beta_0^\eta - \frac{\mathbb{Z}_{66}}{R}\xi_\theta^\eta\right)\\ & + \frac{1}{R}\left(\frac{\mathbb{R}_{66}}{R}\frac{\partial\alpha_0^\eta}{\partial\theta} + \frac{\mathbb{Z}_{66}}{R}\frac{\partial\xi_R^\eta}{\partial\theta} + \mathbb{R}_{66}\frac{\partial\beta_0^\eta}{\partial R} + \mathbb{Z}_{66}\frac{\partial\xi_\theta^\eta}{\partial R} - \frac{\mathbb{R}_{66}}{R}\beta_0^\eta - \frac{\mathbb{Z}_{66}}{R}\xi_\theta^\eta\right)\\ & = I_0^\eta\frac{\partial^2\beta_0^\eta}{\partial t^2} + I_1^\eta\frac{\partial^2\beta_1^\eta}{\partial t^2}\end{aligned} \tag{40b}$$

$$\begin{aligned}\delta w :\ & \frac{\partial}{\partial R}\left(\left(\mathbb{R}_{55}\right)\left(\xi_R^\eta + \frac{\partial\chi_0^\eta}{\partial R}\right)\right) + \frac{1}{R}\frac{\partial}{\partial\theta}\left(\left(\mathbb{R}_{44}\right)\left(\xi_\theta^\eta + \frac{\partial\chi_0^\eta}{R\partial\theta}\right)\right) - \frac{P}{R^2}\frac{\partial^2\chi_0^\eta}{\partial\theta^2}\\ & = \left(I_0\frac{\partial^2\chi_0}{\partial t^2}\right)^\eta\end{aligned} \tag{40c}$$

$$
\begin{aligned}
\delta\xi_R^\eta :\ & \frac{\partial}{\partial R}\left(\left\{\mathbb{Z}_{11}\frac{\partial\alpha_0^\eta}{\partial R}+\mathbb{C}_{11}\frac{\partial\xi_R^\eta}{\partial R}\right\}+\left\{\frac{\mathbb{Z}_{12}}{R}\alpha_0^\eta+\frac{\mathbb{C}_{12}}{R}\xi_R^\eta+\frac{\mathbb{Z}_{12}}{R}\frac{\partial\beta_0^\eta}{\partial\theta}+\frac{\mathbb{C}_{12}}{R}\frac{\partial\xi_\theta^\eta}{\partial\theta}\right\}\right)\\
&-\frac{1}{R}\left(\left\{\mathbb{Z}_{12}\frac{\partial\alpha_0^\eta}{\partial R}+\mathbb{C}_{12}\frac{\partial\xi_R^\eta}{\partial R}\right\}+\left\{\frac{\mathbb{Z}_{22}}{R}\alpha_0^\eta+\frac{\mathbb{C}_{22}}{R}\xi_R^\eta+\frac{\mathbb{Z}_{22}}{R}\frac{\partial\beta_0^\eta}{\partial\theta}+\frac{\mathbb{C}_{22}}{R}\frac{\partial\xi_\theta^\eta}{\partial\theta}\right\}\right)\\
&+\frac{1}{R}\frac{\partial}{\partial\theta}\left(\frac{\mathbb{Z}_{66}}{R}\frac{\partial\alpha_0^\eta}{\partial\theta}+\frac{\mathbb{C}_{66}}{R}\frac{\partial\xi_R^\eta}{\partial\theta}+\mathbb{Z}_{66}\frac{\partial\beta_0^\eta}{\partial R}+\mathbb{C}_{66}\frac{\partial\xi_\theta^\eta}{\partial R}-\frac{\mathbb{Z}_{66}}{R}\beta_0^\eta-\frac{\mathbb{C}_{66}}{R}\xi_\theta^\eta\right)\\
&-\left(\mathbb{R}_{55}\right)\left(\xi_R^\eta+\frac{\partial\chi_0^\eta}{\partial R}\right)=I_1\frac{\partial^2\alpha_0}{\partial t^2}+I_2\frac{\partial^2\xi_R}{\partial t^2}
\end{aligned}
\tag{40d}
$$

$$
\begin{aligned}
\delta\xi_\theta :\ & \frac{1}{R}\frac{\partial}{\partial\theta}\left(\left\{\mathbb{Z}_{12}\frac{\partial\alpha_0^\eta}{\partial R}+\mathbb{C}_{12}\frac{\partial\xi_R^\eta}{\partial R}\right\}+\left\{\frac{\mathbb{Z}_{22}}{R}\alpha_0^\eta+\frac{\mathbb{C}_{22}}{R}\xi_R^\eta+\frac{\mathbb{Z}_{22}}{R}\frac{\partial\beta_0^\eta}{\partial\theta}+\frac{\mathbb{C}_{22}}{R}\frac{\partial\xi_\theta}{\partial\theta}\right\}\right)\\
&+\frac{\partial}{\partial R}\left(\frac{\mathbb{Z}_{66}}{R}\frac{\partial\alpha_0^\eta}{\partial\theta}+\frac{\mathbb{C}_{66}}{R}\frac{\partial\xi_R^\eta}{\partial\theta}+\mathbb{Z}_{66}\frac{\partial\beta_0^\eta}{\partial R}+\mathbb{C}_{66}\frac{\partial\xi_\theta^\eta}{\partial R}-\frac{\mathbb{Z}_{66}}{R}\beta_0^\eta-\frac{\mathbb{C}_{66}}{R}\xi_\theta^\eta\right)\\
&+\frac{1}{R}\left(\frac{\mathbb{Z}_{66}}{R}\frac{\partial\alpha_0^\eta}{\partial\theta}+\frac{\mathbb{C}_{66}}{R}\frac{\partial\xi_R^\eta}{\partial\theta}+\mathbb{Z}_{66}\frac{\partial\beta_0^\eta}{\partial R}+\mathbb{C}_{66}\frac{\partial\xi_\theta^j}{\partial R}-\frac{\mathbb{Z}_{66}}{R}\beta_0^\eta-\frac{\mathbb{C}_{66}}{R}\xi_\theta^\eta\right)\\
&+\frac{1}{R}\left(\frac{\mathbb{Z}_{66}}{R}\frac{\partial\alpha_0^\eta}{\partial\theta}+\frac{\mathbb{C}_{66}}{R}\frac{\partial\xi_R^\eta}{\partial\theta}+\mathbb{Z}_{66}\frac{\partial\beta_0^\eta}{\partial R}+\mathbb{C}_{66}\frac{\partial\xi_\theta^\eta}{\partial R}-\frac{\mathbb{Z}_{66}}{R}\beta_0^\eta-\frac{\mathbb{C}_{66}}{R}\xi_\theta^\eta\right)\\
&-\left(\left(\mathbb{R}_{44}\right)\left(\xi_\theta^\eta+\frac{\partial\chi_0^\eta}{R\partial\theta}\right)\right)=I_1^\eta\frac{\partial^2\beta_0}{\partial t^2}+I_2^\eta\frac{\partial^2\xi_\theta}{\partial t^2}
\end{aligned}
\tag{40e}
$$

where: $\left\{\mathbb{C}_{ij},\mathbb{Z}_{ij},\mathbb{R}_{ij}\right\}=\int_{-\frac{h}{2}}^{\frac{h}{2}}\overline{Q}_{ij}\left\{z^2,z^1,1\right\}dz.$

It is highlighted that, due to the equations of compatibility (Eq. (30)), the amounts of variables which are unknown would be declined from by 8. So, the total amounts of unknowns in the core and face sheets is reduced from 25 to 13.

9 Solution process

Recently, computer aid simulation and semi numerical approach become well-known to simulation different problems [94–102]. In this stage of the current paper, we introduce a solution procedure called GDQM to solve the formulation of the current problem. In this method have:

$$
\left.\frac{\partial f}{\partial r}\right|_{r=r_i,\,\theta=\theta_j}=\sum_{m=1}^{N_r}\sum_{n=1}^{N_\theta}A_{im}^r I_{jn}^\theta f_{mn}
\tag{41a}
$$

$$
\left.\frac{\partial f}{\partial \theta}\right|_{r=r_i,\,\theta=\theta_j}=\sum_{m=1}^{N_r}\sum_{n=1}^{N_\theta}I_{im}^r A_{jn}^\theta f_{mn}
\tag{41b}
$$

$$
\frac{\partial}{\partial r}\left(\left.\frac{\partial f}{\partial \theta}\right|_{r=r_i,\,\theta=\theta_j}\right)=\sum_{m=1}^{N_r}\sum_{n=1}^{N_\theta}A_{im}^r A_{jn}^\theta f_{mn}
\tag{41c}
$$

$$
\left.\frac{\partial^2 f}{\partial r^2}\right|_{r=r_i,\,\theta=\theta_j}=\sum_{m=1}^{N_r}\sum_{n=1}^{N_\theta}B_{im}^r I_{jn}^\theta f_{mn}
\tag{41d}
$$

$$
\left.\frac{\partial^2 f}{\partial \theta^2}\right|_{r=r_i,\,\theta=\theta_j}=\sum_{m=1}^{N_r}\sum_{n=1}^{N_\theta}I_{im}^r B_{jn}^\theta f_{mn}
\tag{41e}
$$

Also, I_{im}^r and I_{jn}^θ would equal to 1 while $m=i$ and $n=j$ otherwise, may be equal to *0*. Furthermore, B_{jn}^θ, B_{im}^r, A_{jn}^θ and A_{im}^r may be weighting factors of the second and first-order derivatives along with the θ and r orientation, respectively, and would be taken into consideration as

$$A_{im}^{(1)}=\begin{cases}\frac{\xi(r_i)}{(r_i-r_m)\xi(r_m)} & when \quad i\neq m\\ -\sum_{k=1,k\neq i}^{N_r}A_{ik}^{(1)} & when \quad i=m\end{cases}\qquad i,m=1,2,\ldots,N_r \tag{42a}$$

$$A_{jn}^{(1)}=\begin{cases}\frac{\xi(\theta_j)}{(\theta_j-\theta_n)\xi(\theta_n)} & when \quad j\neq n\\ -\sum_{k=1,k\neq j}^{N_\theta}A_{jk}^{(1)} & when \quad j=n\end{cases}\qquad j,n=1,2,\ldots,N_\theta \tag{42b}$$

in which

$$\xi(r_i)=\prod_{k=1,k\neq i}^{N_r}(r_i-r_k) \tag{43a}$$

$$\xi(\theta_j)=\prod_{k=1,k\neq j}^{N_\theta}(\theta_j-\theta_k) \tag{43b}$$

And

$$B_{im}^{(r)}=r\left(A_{ii}^{(r-1)}A_{im}^{(1)}-\frac{A_{im}^{(r-1)}}{(r_i-r_m)}\right)\quad i,m=1,2,\ldots,N_r\ ,\ i\neq m \tag{44a}$$

$$B_{jn}^{(\theta-1)}=\theta\left(A_{jj}^{(\theta-1)}A_{jn}^{(1)}-\frac{A_{jn}^{(\theta-1)}}{(\theta_j-\theta_n)}\right)\quad j,n=1,2,\ldots,N_\theta\ ,\ j\neq n \tag{44b}$$

$$B_{ii}^{(r)}=-\sum_{k=1,k\neq i}^{N_r}B_{ik}^{(r)}\quad ,\ i=1,2,\ldots,N_r\ ,\ i=m \tag{44c}$$

$$B_{jj}^{(\theta)}=-\sum_{k=1,k\neq j}^{N_\theta}B_{jk}^{(\theta)}\quad ,\ j=1,2,\ldots,N_\theta\ ,\ j=n \tag{44d}$$

In addition, applying points of Chebyshev polynomials greed, the seed as well as r and θ directions would be distributed as [103]

Table 1 Comparison of non-dimensional natural frequency ($\overline{\omega}^2=\omega b^2\sqrt{\rho/E}$) of the multi-scale nanocomposite face sheets for different CNT pattern

CNT distribution	V_{CNT}			
	0.04		0.06	
	Current research	Ref . [108]	Current research	Ref . [108]
FG-X	3.2647	3.2604	3.4805	3.4808
FG-V	3.3775	3.3817	3.5795	3.5783
FG-A	3.4275	3.4291	3.6292	3.6294
FG-UD	3.4174	3.4156	3.6197	3.6170

Table 2 The material properties of core [18] and composite layer [109]

CNTs	Matrix (Epoxy)	Fiber (Carbon)	Metal (Core)
$\vartheta_{12}=0.33$	$E^m(Gpa)=3.51$	$\upsilon^f=0.2$	$\nu^s=0.34$
$\rho^{cnt}(kg/m^3)=1350$	$\nu^m=0.34$	$\rho^f(\frac{kg}{m^3})=1750$	$\rho^s(\frac{kg}{m^3})=2700$
$E^{cnt}(Gpa)=640$	$\rho^m(\frac{kg}{m^3})=1200$	$E_{11}^f(GPa)=233.05$	$E^s(Gpa)=70$
$d^{cnt}(m)=1.4\times10^{-9}$		$E_{11}^f(GPa)=23.1$	
$t^{cnt}(m)=0.34\times10^{-9}$		$G_{11}^f(GPa)=8.96$	
$l^{cnt}(m)=25\times10^{-6}$			

Table 3 Convergence study of the GDQM for solving the current research for different boundary conditions (B.Cs)

B.Cs	$N=4$	$N=6$	$N=8$	$N=10$	$N=12$	$N=14$
S–S	0.0370	0.0419	0.0421	0.0422	0.0422	0.0422
C-S	0.1015	0.1009	0.1009	0.1009	0.1009	0.1009
C–C	0.1398	0.1390	0.1385	0.1385	0.1385	0.1385

Table 4 Convergence study of the GDQM for solving the current research for different CNT-distribution pattern and PD

PD	CNT- distribution	Nt = 2	Nt = 4	Nt = 6	Nt = 8	Nt = 10	Nt = 12	Nt = 14	Nt = 16	Nt = 100
X	FG-X	0.1385	0.1363	0.1370	0.1373	0.1374	0.1374	0.1374	0.1375	0.1375
	FG-O	0.1411	0.1354	0.1349	0.1347	0.1347	0.1346	0.1346	0.1346	0.1346
	FG-UD	0.1401	0.1358	0.1358	0.1358	0.1357	0.1357	0.1357	0.1357	0.1358
O	FG-X	0.1247	0.1360	0.1363	0.1363	0.1363	0.1363	0.1363	0.1363	0.1363
	FG-O	0.1286	0.1344	0.1346	0.1346	0.1346	0.1346	0.1346	0.1346	0.1347
	FG-UD	0.1275	0.1349	0.1351	0.1351	0.1351	0.1351	0.1351	0.1351	0.1351
UD	FG-X	0.1325	0.1352	0.1358	0.1359	0.1360	0.1360	0.1361	0.1361	0.1361
	FG-O	0.1357	0.1342	0.1338	0.1338	0.1337	0.1337	0.1337	0.1337	0.1337
	FG-UD	0.1346	0.1346	0.1346	0.1346	0.1346	0.1346	0.1346	0.1346	0.1346

Table 5 Effects of three types' method for reinforcing the structure on the system's frequency with consideration three porosity coefficient and boundary conditions

	Simply-Simply			Clamped-Simply			Clamped–Clamped		
	FG-X	FG-O	FG-UD	FG-X	FG-O	FG-UD	FG-X	FG-O	FG-UD
Without imperfection ($e_0 = 0$)									
MHC/HC/MHC[1]	0.0388	0.0378	0.0381	0.09[illegible]	0.0918	0.0926	0.1296	0.1263	0.1275
CNT/HC/CNT[2]	0.0489	0.0395	0.0465	0.0825	0.0697	0.0785	0.1190	0.9998	0.1155
With imperfection ($e_0 = 0.3$)									
MHC/HC/MHC[1]	0.0396	0.0386	0.03[illegible]	0.0961	0.0938	0.0946	0.1322	0.1291	0.1302
CNT/HC/CNT[2]	0.0451	0.0321	0.0407	0.0[illegible]75	0.0594	0.0702	0.1140	0.0895	0.1042
With imperfection ($e_0 = 0.5$)									
MHC/HC/MHC[1]	0.0406	0.0396	0.0400	0.0984	0.0963	0.0971	0.1355	0.1325	0.1337
CNT/HC/CNT[2]	0.0556	0.0407	0.0507	0.0950	0.0732	0.0842	0.1329	0.1042	0.1258

[1]Multi-scale hybrid nanocomposite reinforced disk /Honey-Comb/ Multi-scale hybrid nanocomposite reinforced disk

[2]Carbon nanotubes reinforced disk/Honey-Comb/ Carbon nanotubes reinforced disk

$$r_i = \frac{-R_i + R_0}{2}\left(-\cos\left(\frac{(i-1)}{(N_r-1)}\pi + 1\right)\right) + R_i \quad i = 1, 2, 3, \ldots, N_r \tag{45a}$$

$$\theta_j = \left(-\cos\left(\frac{(j-1)}{(N_\theta - 1)}\pi + 1\right)\right)\frac{\chi}{2} \quad j = 1, 2, 3, \ldots, N_\theta \tag{45b}$$

By employing the GDQM as solution method of this problem, an algebraic eigenvalue [79, 104–107] would be created. These relations would be given by:

$$\left\{\begin{bmatrix} [M_{dd}] & [M_{db}] \\ [M_{bd}] & [M_{bb}] \end{bmatrix}\omega_n^2 + \begin{bmatrix} [K_{dd}] & [K_{db}] \\ [K_{bd}] & [K_{bb}] \end{bmatrix}\right\}\left\{\begin{matrix} \delta_d \\ \delta_b \end{matrix}\right\} = 0 \tag{46}$$

Eventually, Though Eq. (46) the novel system are

$$[K_{dd}]\delta_d + [K_{db}]\delta_b = 0 \tag{47a}$$

$$[K_{bd}]\delta_d + [K_{bb}]\delta_b = 0 \tag{47b}$$

here, the freedom degrees' vector will be expressed as:

$$\delta_b = -\delta_d \frac{[K_{dd}]}{[K_{db}]} \tag{48}$$

By inserting of Eq. (48) into Eq. (47b):

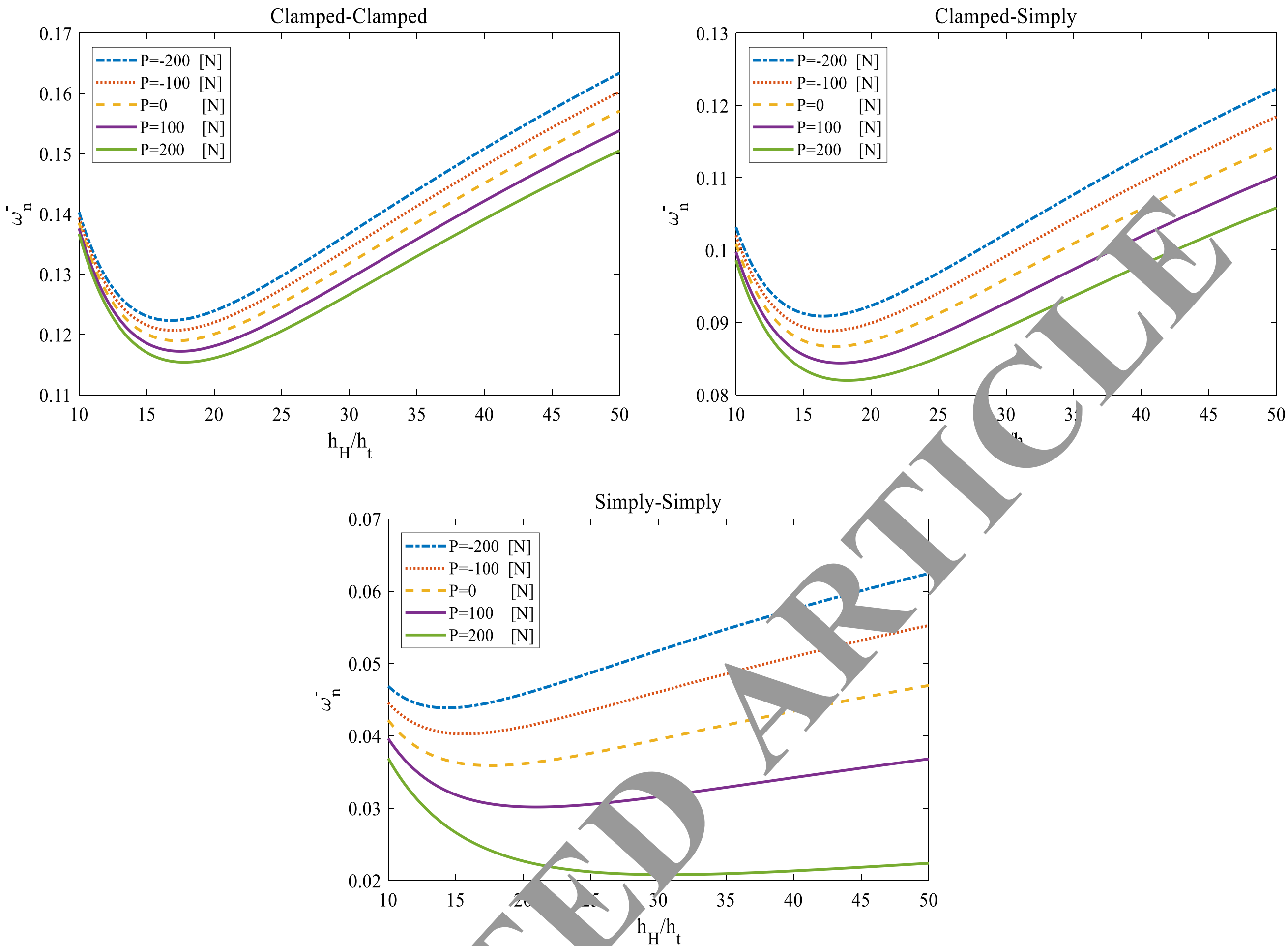

Fig. 4 Frequency of the disk versus to the honeycomb core to composite face-sheet thickness ratio for five value of internal force and three kinds of boundary conditions

$$\left(-[K_{bb}][K_{db}]^{-1}[K_{dd}] + [K_{bd}]\right)\delta_d = 0 \tag{49}$$

So

$$K^* = [K_{bd}] - [K_{bb}][K_{db}]^{-1}[K_{dd}] \tag{50}$$

and

$$[M_{bd}]\delta_d + [M_{bb}]\delta_b = 0 \tag{51}$$

Also, by applying of Eq. (48) into Eq. (51):

$$\left(-[M_{bb}][K_{db}]^{-1}[K_{dd}] + [M_{bd}]\right)\delta_d = 0 \tag{52}$$

Thereby

$$M^* = -[M_{bb}][K_{db}]^{-1}[K_{dd}] + [M_{bd}] \tag{53}$$

Ultimately, through solving the following relation, the structure's displacement fields and frequency information would be derived by GDQM.

$$M^*\omega^2 + K^* = 0 \tag{54}$$

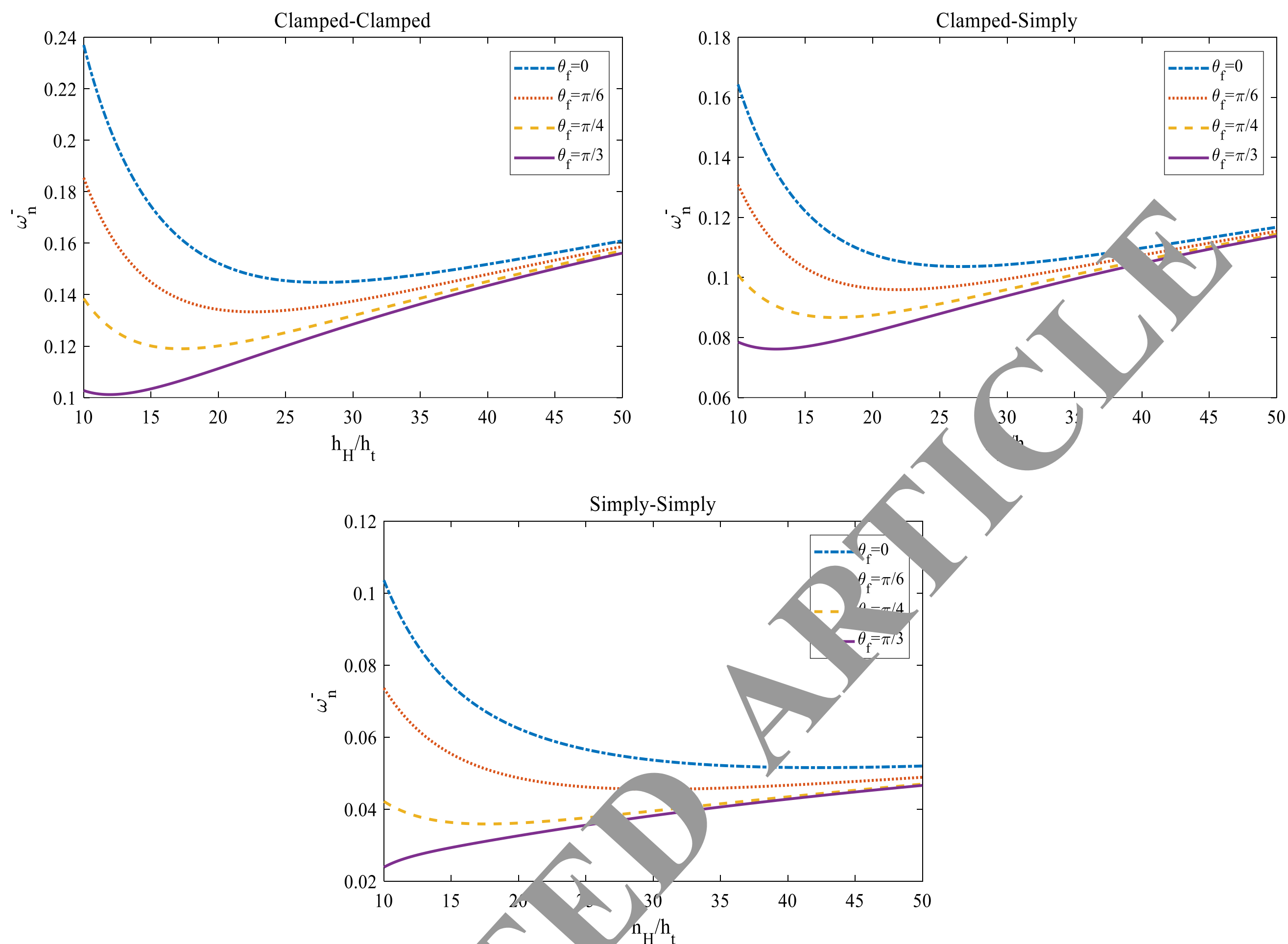

Fig. 5 Frequency of the disk versus to the honeycomb core to composite face-sheet thickness ratio for three kinds of boundary conditions and four θ_f

10 Results and discussion

For evaluating the reliability of the current method, the dimensionless natural frequency of the annular plate obtained in this research is compared with outcomes provided by Ref. [108] in Table 1. As illustrated in a broad range of W_{CNT} and CNT-distribution pattern, there is a good agreement between the outcomes. Regarding the table, this study anticipates the vibration characteristics of the annular plate very close and similar to the outcomes given in Ref. [108].

The mechanical properties for both of the reinforcements (Carbon Fiber and Carbon nanotube) and the epoxy matrix are shown in Table 2.

Also, the properties of SMA and matrix layer illustrated in Ref. [48]. Convergence number of grid points for having independent results with respect to the three kinds of boundary conditions is investigated in Table 3. As illustrated in Table 3, as grid points' number in the GDQ approach is more than eleven, the error for the calculation of the disk's natural frequency becomes zero and this matter is a fact for all boundary conditions.

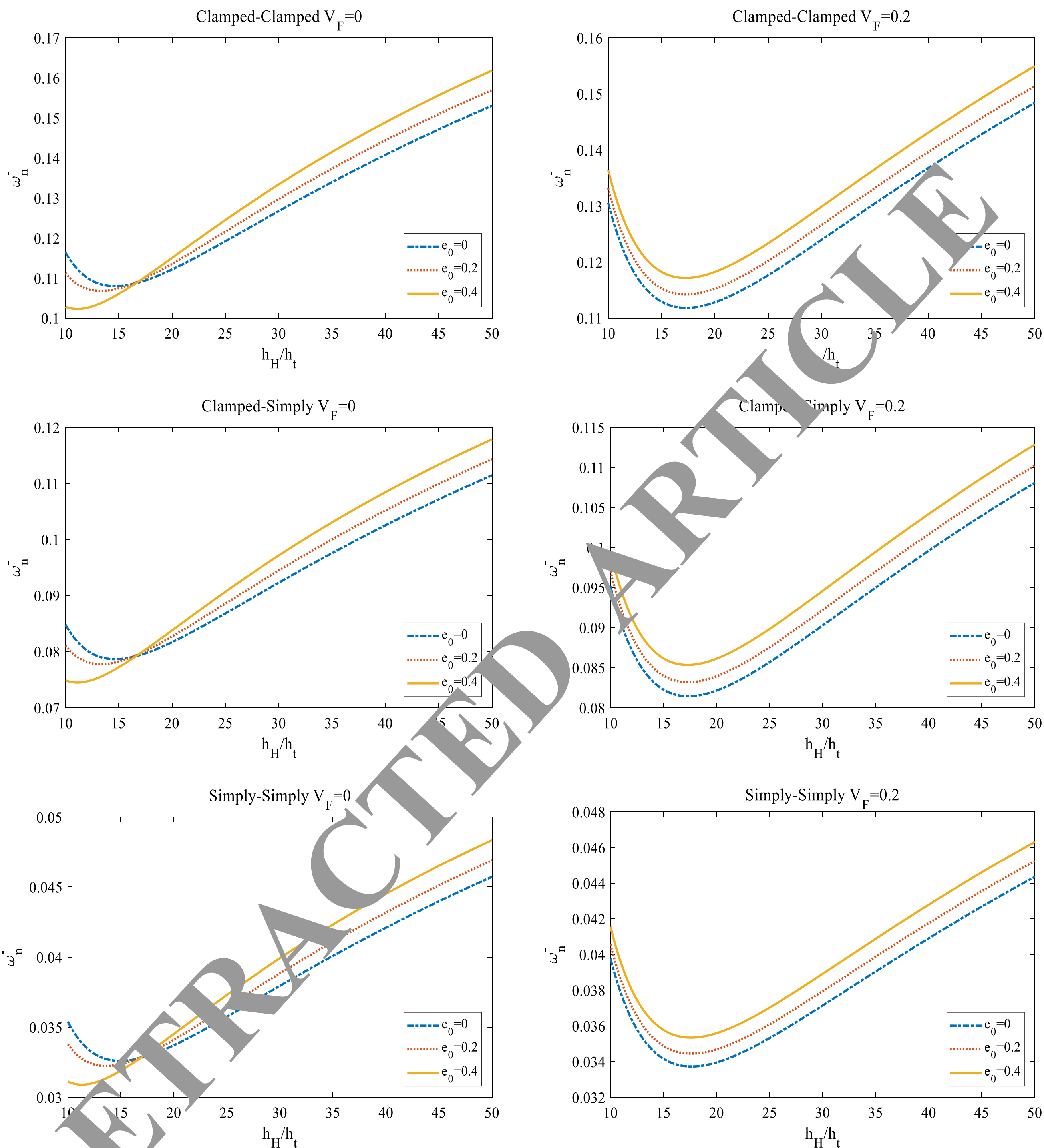

Fig. 6 Frequency of the disk versus to h_H/h_t for three kinds of boundary conditions

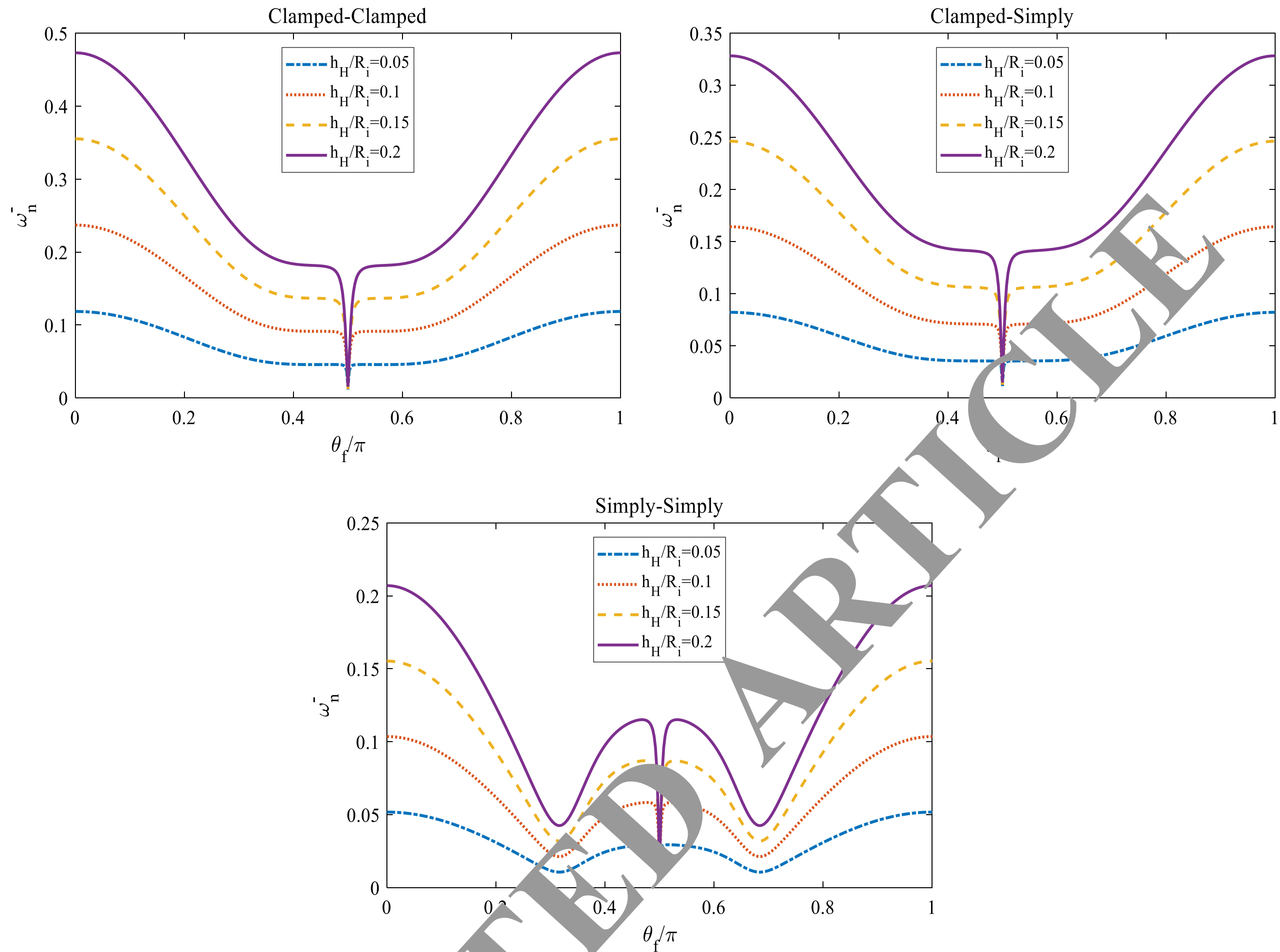

Fig. 7 Frequency of the disk versus to θ_f/π for three kinds of boundary conditions and four h_H/R_i

Convergence information for effect of the number of nanocomposite layer (Nt) and various functionally graded distribution on the frequency of the multi-phase disk with respect to the porosity patterns is depicted in Table 4.

Based on Table 4, we can state that the structure will have the best dynamic response by considering the PD-X and FG-O pattern, also the layer's number in the compositionally face sheets must not exceed nine for all FG and porosity patterns, due to the $Nt \geq 10$ we are not able to observe any change in the structure's frequency. Analysis of the impact of three types' method for reinforcing the structure on the system's frequency with consideration three porosity coefficient and boundary conditions is argued in Table 5. The ends of Table 5 are that for clamped-simply, and clamped–clamped not only MHC/HC/MHC reinforced disk have the greatest natural frequency compared to CNTs/HC/CNTs reinforcements but also growing the imperfection effect is a reason to decrease the systems' frequency.

In accord with Table 5, it can be concluded that applying the honeycomb network as the core of the structure will enhance the structure's dynamic response, impressively. The graphs and data in Fig. 4 depicts the internal force, three types of boundary conditions, and honeycomb core to composite face-sheet thickness ratio (h_H/h_t) effects on the vibrational response of the compositionally disk. It is as a fact

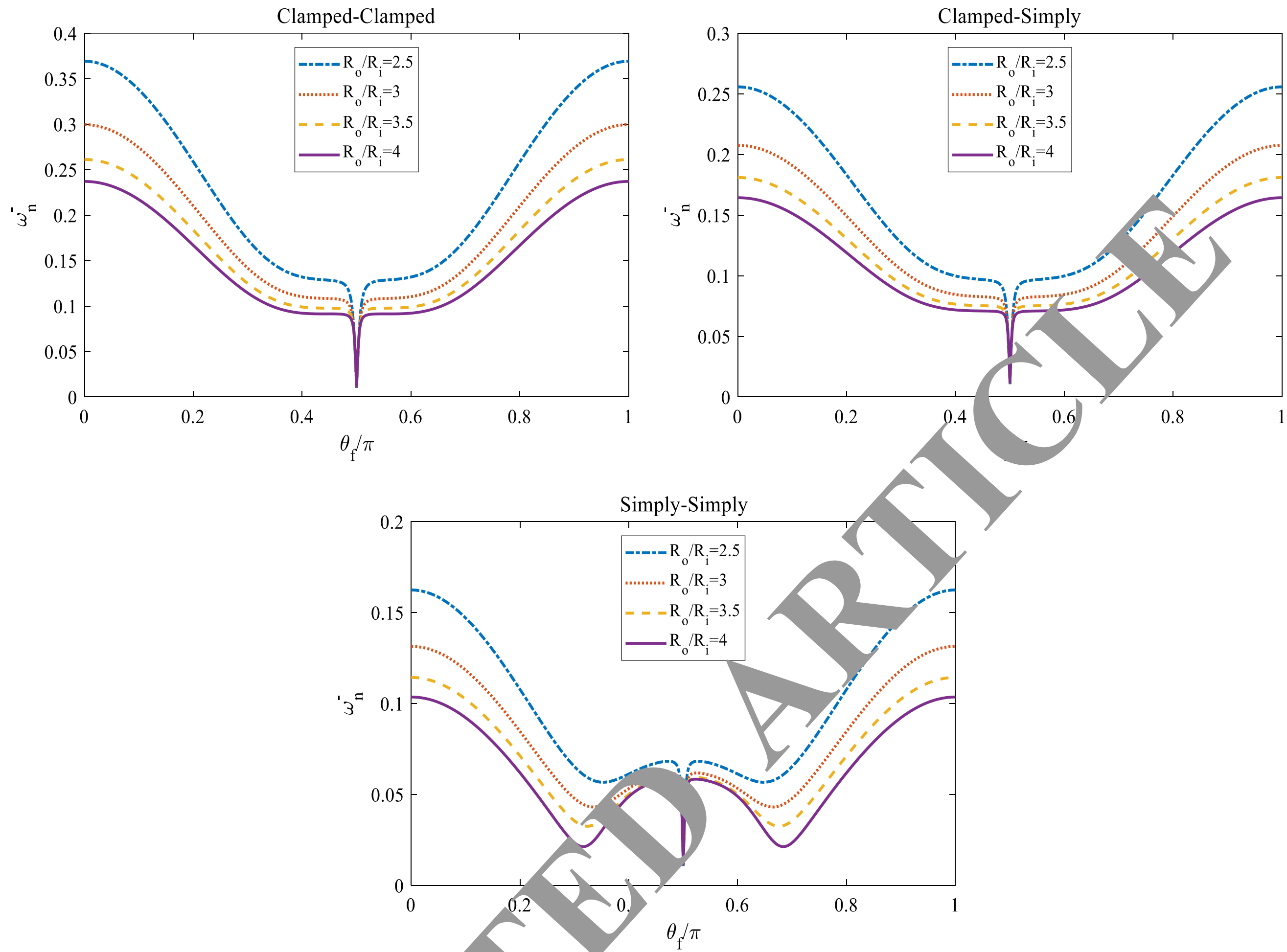

Fig. 8 Frequency of the disk versus to $\frac{\theta_f}{\pi}$ for three kinds of boundary conditions and four R_o/R_i

for various boundary condition in which with each increase in the applied internal force can claim that the frequency of the structure tends to improve, particularly in the bigger value of h_H/h_t and simply-simply boundary conditions. For each boundary condition and any value of internal pressure, the relation between h_H/h_t and the sandwich structure's frequency is the same as quadratic function. For more explanation by ever-increasing in the h_H/h_t at first, the honeycomb core structure's frequency drops, exponentially and after a specific value for the h_H/h_t the structure's dynamic response improves, linearly.

The Fig. 9 illustrates the fibers angel (θ_f), three types of boundary conditions, and honeycomb core to composite face-sheet thickness ratio (h_H/h_t) effects on the vibrational behaviors of the compositionally disk. It is as a fact for various boundary condition in which with each decrease in the θ_f can claim that the frequency of the structure tends to improve, particularly for the smaller values of h_H/h_t and simply-simply boundary conditions. Also, the impact of the fibers angle on the frequency can be overlooked for large h_H/h_t. For each boundary conditions and any value of fibers angel, the relation among h_H/h_t and the sandwich structure's frequency is the same as quadratic function. To clarify it more, by ever-increasing in the h_H/h_t at first, the honeycomb core structure's frequency drops, exponentially and after the specific value of the structure' dynamic response improves, linearly. It is important to mention that the specific value for the h_H/h_t grows by increasing the θ_f.

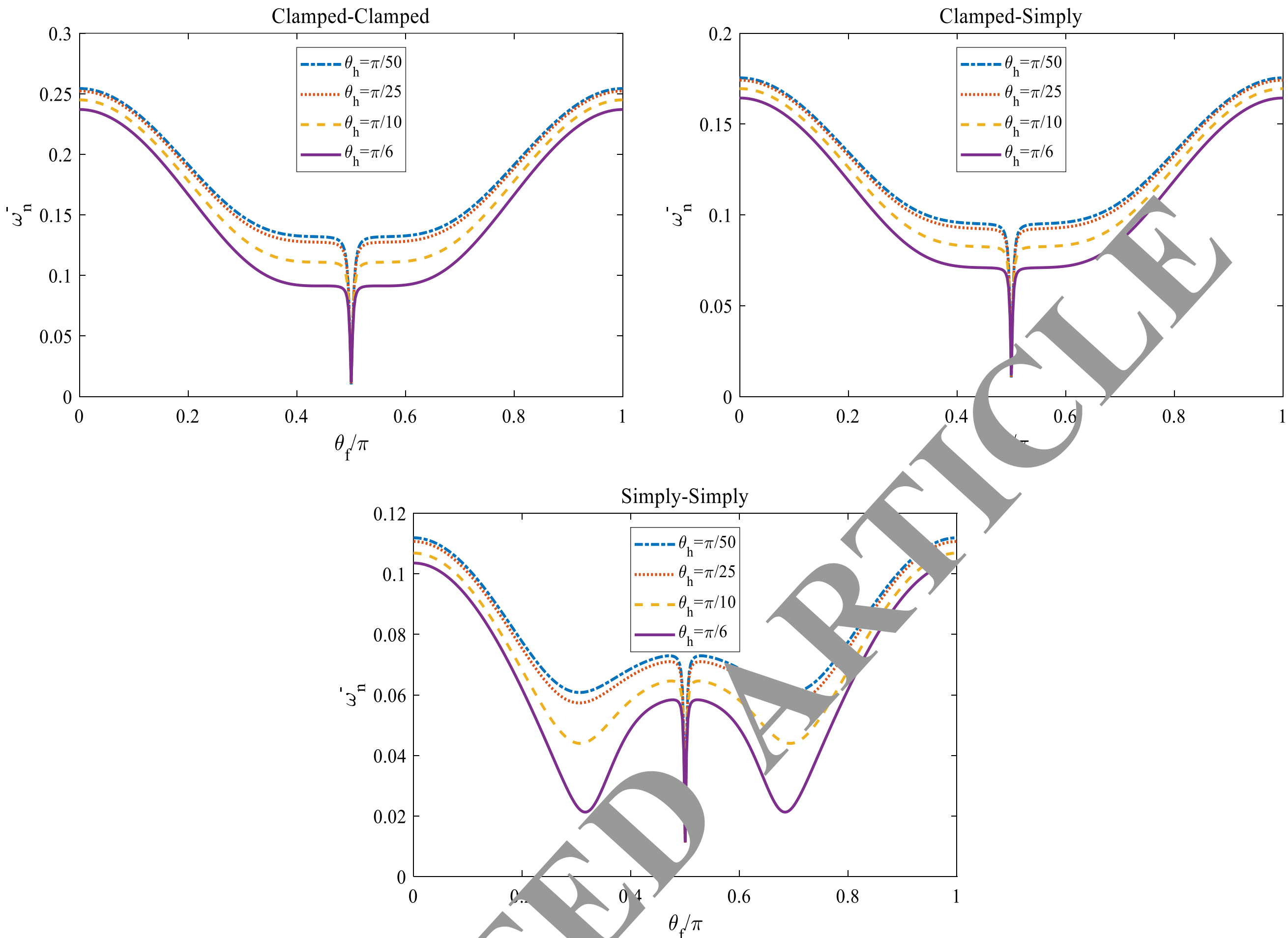

Fig. 9 Frequency of the disk versus to $\frac{\theta_f}{\pi}$ for three kinds of boundary conditions and four θ_h

The depicted graph in Fig. 6 displays the fibers angel (V_f), three types of boundary conditions, porosity factor, and honeycomb core to composite thickness ratio of face sheet (h_H/h_t) effects on the vibrational behaviors of the compositionally disk. As common result in all below figure by ever-increasing in the h_H/h_t at first, the honeycomb core structure's frequency drops exponentially and after the specific value the structure's dynamic response improves, linearly.

Figure 7 shows that the fibers angel (θ_f/π), three types of boundary conditions, and honeycomb core thickness to inner radius ratio (h_H/R_i) effects on the vibrational behaviors of the compositionally disk. As Fig. 7 presents the relation between fibers angle and frequency is similar to a bell-shaped function with the positive concave. When the θ_f/π becomes close to 0.5, there is no change in the disk's frequency, especially for the smaller h_H/R_i and C–C and C-S boundary conditions. In addition, for each value of θ_f/π, dynamic stability of the structure will improve by increasing h_H/R_i. As another general outcome, the critical or minimum frequency for the sandwich disk displays when the $(\theta_f/\pi)^{C-C}$ and $(\theta_f/\pi)^{C-S}$ are 0.5 while for S–S edges, θ_f/π is equal to 0.5, 0.32, and 0.64.

The given information in Fig. 8 shows the fibers angel (θ_f/π), three kinds of boundary conditions, and outer to inner radius ratio (R_o/R_i) affect the vibrational behavior of the compositionally disk. Figure 8 presents that each value

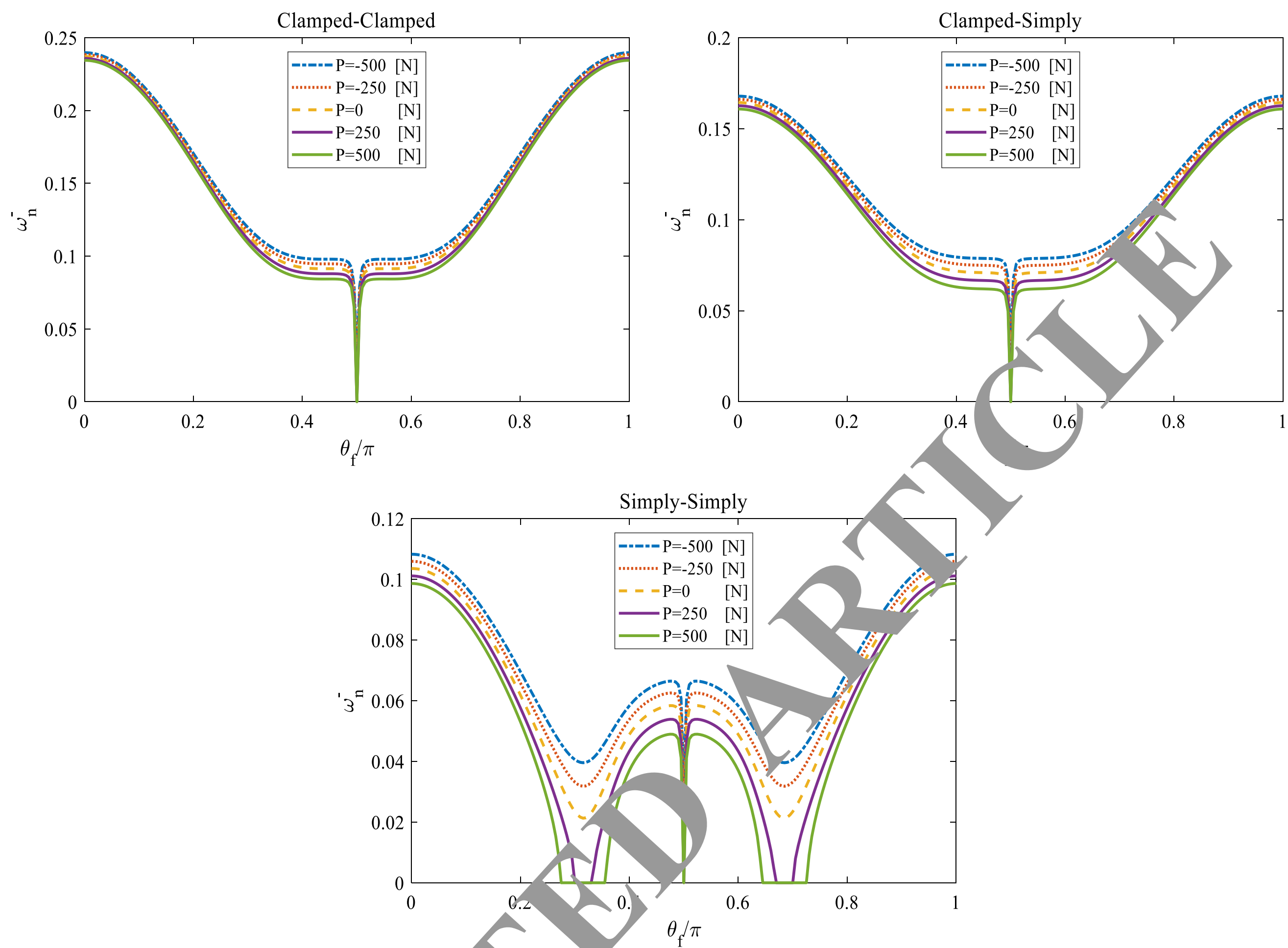

Fig. 10 Frequency of the disk versus to θ_f/π for three kinds of boundary conditions and four p

of θ_f/π, the structure's dynamic stability will improve through an increase in R_i parameter.

The given information in Fig. 9 shows the fibers angel (θ_f/π), three types of boundary conditions, and honeycomb network angel (θ_h) affect the vibrational behaviors of the compositionally disk. As Fig. 9 depicts by considering the close angles for honeycomb network, θ_h have significant role in the disk's frequency as an enhancement.

The Fig. 10 indicates that the fibers angel (θ_f/π), three kinds of boundary conditions, and external applied load (p) effects on the vibrational behaviors of the compositionally disk. By considering external applied load, the impact of compressive or tensile load on the structure's dynamic response is impressive as the rigidity of the edges decreases and the dimensionless fibers angle becomes close to 0.5. As a remarkable result, when the structure is encountered with clamped edges, there is a critical fibers angel in which is equal to 0.5, but if we consider pure simply edges and compressive load, there can see three critical fibers angels in which are equal to 0.5, 0.33, and 0.66. In addition, by considering tensile applied load there is a range for critical fibers angel and this range expands by increasing the value of applied load.

Figure 11 depicts the effects of three types of boundary conditions, various thickness of the SMA reinforced face

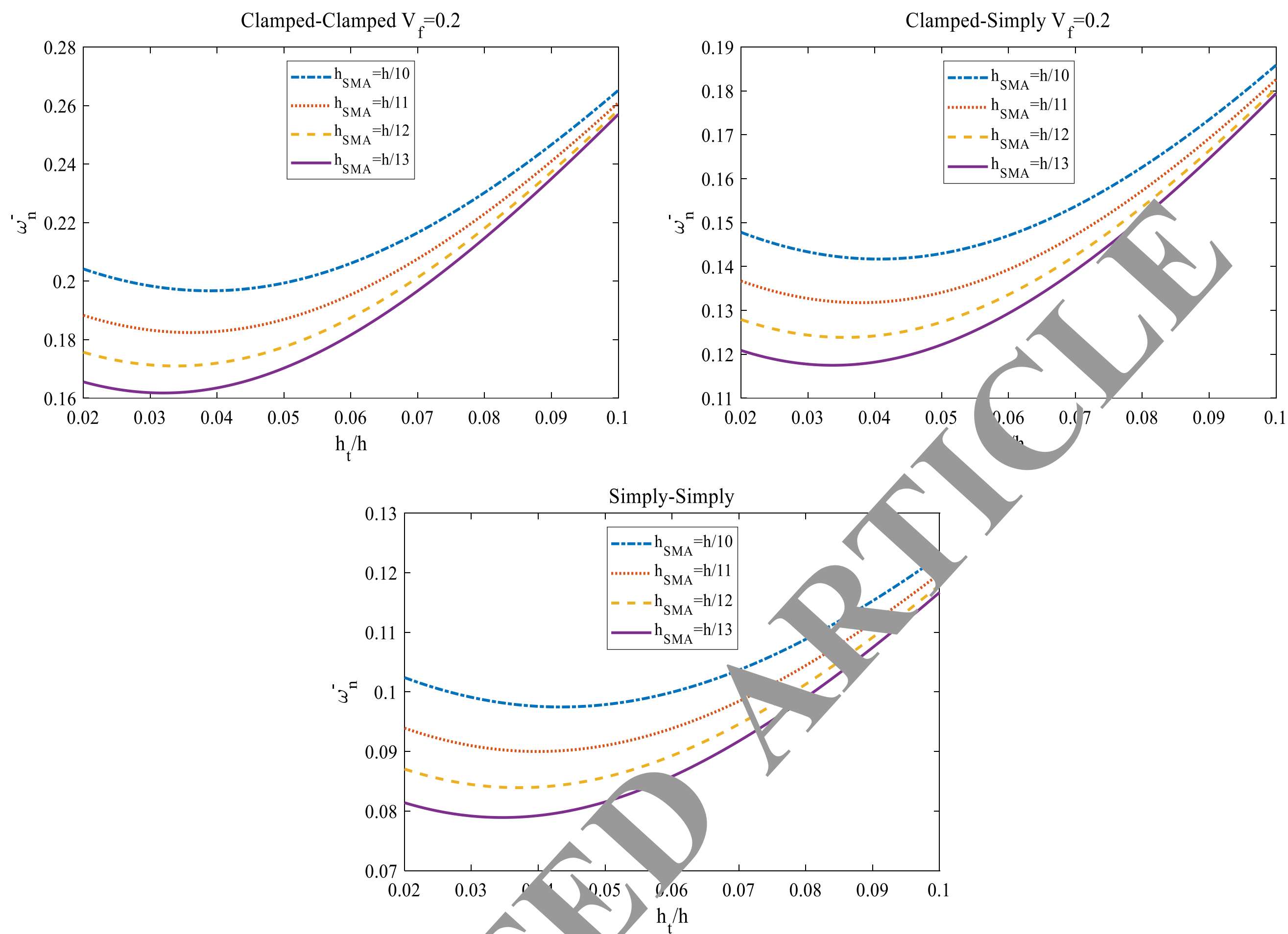

Fig. 11 Frequency of the sandwich disk versus to h_t/h for three kinds of boundary conditions and four h_{SMA}

sheet (h_{SMA}), and MHC face sheet to total thickness ratio (h_t/h) on the vibrational response of the compositionally disk. For various boundary condition, with each increase in the h_{SMA} parameter the frequency of the structure tends to improve, particularly in the lowest value of h_t/h and simply-simply boundary condition. Also, for boundary conditions and h_{SMA} values, the relation between h_t/h and sandwich structure's frequency is the same as quadratic function. To clarify it, by ever-increasing in the h_t/h at first the honeycomb core structure's frequency drops, exponentially and after an specific value for the h_t/h the dynamic response of the structure improves.

In Fig. 12 shows the effects of three boundary condition types, various SMA (V_S) value fraction, and MHC face sheet to total thickness ratio (h_t/h) on the vibrational response of the compositionally disk. For various boundary condition, with each increase in the V_S parameter the frequency of the structure tends to improve. As an important report, the impact of V_S element on the dynamics of the structure is more considerable at the initial h_t/h value.

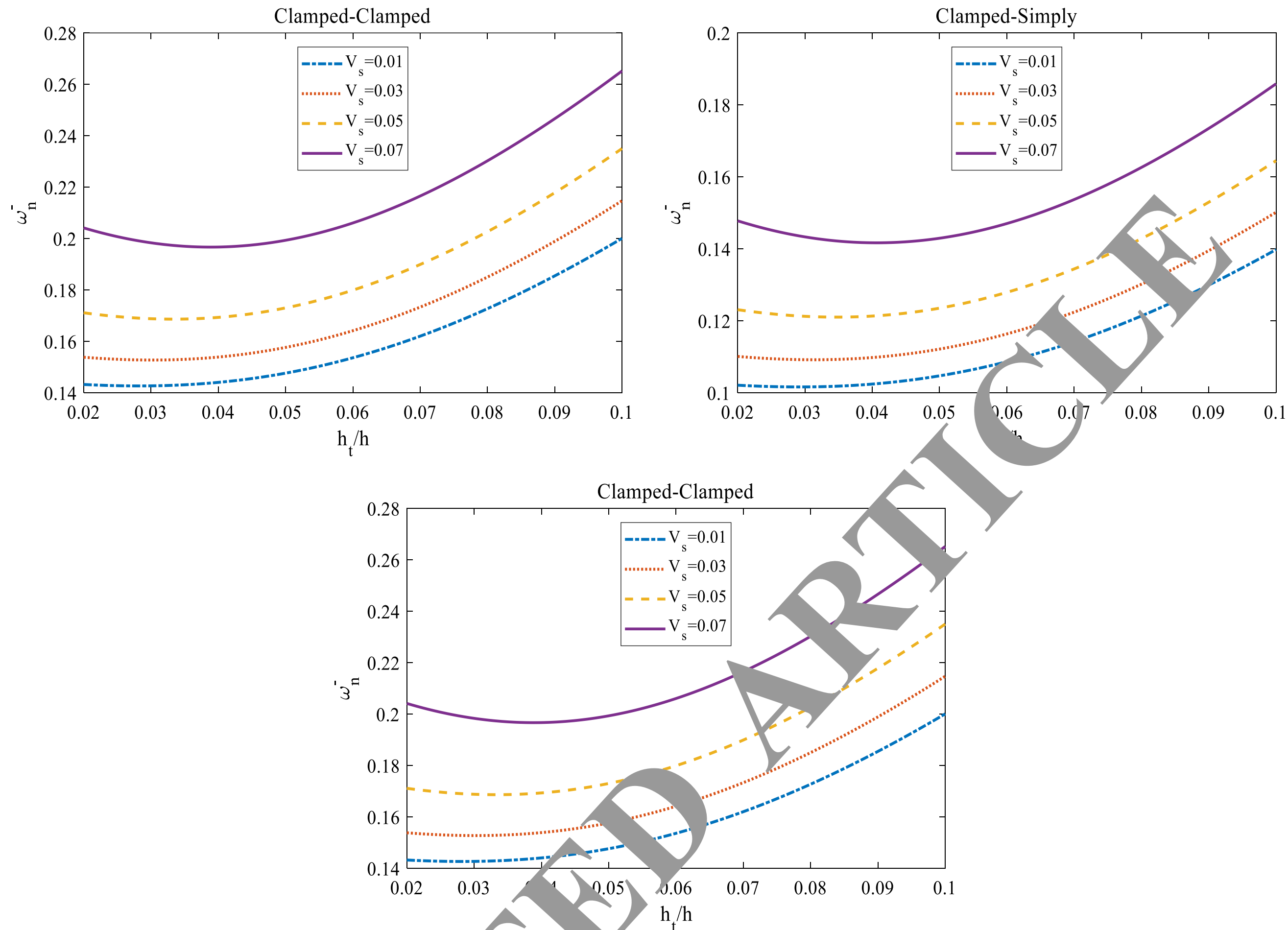

Fig. 12 Frequency of the sandwich disk versus h_t/h parameter for three kinds of boundary conditions and four V_S

11 Conclusion

A porous sandwich disk's vibrational specifications with a core (honeycomb), two middle layers including SMA fiber, and two outer layers of MHC under in-plane pressure is studied. By employing FSDT, the stress and strain relations are acquired. Halpin's modified model–Tsai and the mixture rule are combined to provide the efficient material constant of the introduced porous sandwich structure. Eventually, the key results of this study are as follows:

- for each boundary conditions and internal pressure's values, the relation among sandwich structure' frequency and h_H/h_t is as same as quadratic function.
- As an important report, the impact of V_S element on the dynamics of the structure is more considerable at the initial h_t/h value.
- For boundary conditions and h_{SMA} values, the relation between sandwich structure's frequency and h_t/h is as same as quadratic function.
- for various boundary conditions, with each increase in the h_{SMA} parameter the frequency of the structure tends to improve, particularly in the lowest value of h_t/h and simply-simply boundary conditions.
- the effect of the fibers angle on the frequency can be overlooked for lager value of h_H/h_t
- For various boundary condition, with each increase in the h_{SMA} parameter the frequency of the structure tends to improve, particularly in the lowest value of h_t/h and simply-simply boundary conditions
- By an increase in the h_H/h_t at first, the honeycomb core structure's frequency drops, exponentially and after the specific value of the structure's dynamic response improves, linearly.
- when the θ_f/π parameter becomes close to $\pi/2$, there is no change in the disk's frequency, especially for the smaller value of h_H/R_i and C–C boundary conditions.
- by considering external applied load, the impact of compressive or tensile load on the structure's dynamic response is impressive as the edges' rigidity decreases and the dimensionless fibers angle becomes close to $\pi/2$.

References

1. Chen S, Hassanzadeh-Aghdam M, Ansari R (2018) An analytical model for elastic modulus calculation of SiC whisker-reinforced hybrid metal matrix nanocomposite containing SiC nanoparticles. J Alloy Compd 767:632–641
2. Gao N, Cheng B, Hou H, Zhang R (2018) Mesophase pitch based carbon foams as sound absorbers. Mater Lett 212:243–246
3. Yan H, Xue X, Chen W, Wu X, Dong J, Liu Y, Wang Z (2020) Reversible na+ insertion/extraction in conductive polypyrrole-decorated nati2 (po4) 3 nanocomposite with outstanding electrochemical property. Appl Surf Sci 530:147295
4. Guo H, Qian K, Cai A, Tang J, Liu J (2019) Ordered gold nanoparticle arrays on the tip of silver wrinkled structures for single molecule detection. Sensors Actuators B Chem 300:126846
5. Cai C, Wu X, Liu W, Zhu W, Chen H, Qiu JCD, Sun C-N, Liu J, Wei Q, Shi Y (2020) Selective laser melting of near-α titanium alloy Ti-6Al-2Zr-1Mo-1V: Parameter optimization, heat treatment and mechanical performance. J Mater Sci Technol
6. Lin J, Hu J, Wang W, Liu K, Zhou C, Liu Z, Kong S, Lin S, Deng Y, Guo Z (2020) Thermo and light-responsive strategies of smart titanium-containing composite material surface for enhancing bacterially anti-adhesive property. Chem Eng J 125783
7. Cai C, Gao X, Teng Q, Kiran R, Liu J, Wei Q, Shi Y (2020) Hot isostatic pressing of a near α-Ti alloy: Temperature optimization, microstructural evolution and mechanical performance evaluation. Materials Science and Engineering: A:140426
8. Gao N, Hou H, Wu JH (2018) A composite and deformable honeycomb acoustic metamaterial. Int J Mod Phys B 32(20):1850204
9. Ni T, Yao Y, Chang H, Lu L, Liang H, Yan A, Huang Z, Wen X (2019) LCHR-TSV: Novel low cost and highly repairable honeycomb-based TSV redundancy architecture for clustered faults. IEEE Transactions on Computer-Aided Design of Integrated Circuits and Systems
10. Shariati M, Mafipour MS, Mehrabi P, Shariati A, Toghroli A, Trung NT, Salih MN (2020) A novel approach to predict shear strength of tilted angle connectors using artificial intelligence techniques. Eng Comput 1–21
11. Wu Q, Chen H, Gao W (2019) Nonlocal strain gradient forced vibrations of FG-GPLRC nanocomposite microbeams. Eng Comput 1–12
12. Mukhopadhyay T, Adhikari S (2016) Free-vibration analysis of sandwich panels with randomly irregular honeycomb core. J Eng Mech 142(11):06016008. https://doi.org/10.1061/(ASCE)EM.1943-7889.0001153
13. Suryawanshi VJ, [illegible] AS, [illegible]alekar SP, Rade KA (2020) Defect detection of composite honeycomb structure by vibration analysis technique. Materials Today: Proceedings. https://doi.org/10.1016/j.matpr.2019.12.192
14. Mozafari H, Najafian S (2019) Vibration analysis of foam filled honeycomb sandwich panel–numerical study. Aust J Mech Eng 17(3):[illegible]–198
15. Xu G-d, Zeng T, Cheng S, Wang X-h, Zhang K (2019) Free vibration of composite sandwich beam with graded corrugated lattice core. Compos Struct 229:111466. https://doi.org/10.1016/j.compstruct.2019.111466
16. Amini A, Mohammadimehr M, Faraji A (2019) Active control to reduce the vibration amplitude of the solar honeycomb sandwich panels with CNTRC facesheets using piezoelectric patch sensor and actuator. Steel Compos Struct 32 (5):671–686. https://doi.org/10.12989/scs.2019.32.5.671
17. Shahverdi H, Barati MR, Hakimelahi B (2019) Post-buckling analysis of honeycomb core sandwich panels with geometrical imperfection and graphene reinforced nano-composite face sheets. Mater Res Express 6(9):095017
18. Sobhy M (2020) Differential quadrature method for magneto-hygrothermal bending of functionally graded graphene/Al sandwich-curved beams with honeycomb core via a new higher-order theory. J Sandwich Struct Mater https://doi.org/10.1177/1099636219900668
19. Wang Y-j, Zhang Z-j, Xue X-m, Zhang L (2019) Free vibration analysis of composite sandwich panels with hierarchical honeycomb sandwich core. Thin-Walled Struct 145:106425
20. Zhang Z-j, Han B, Zhang Q-c, Jin F (2017) Free vibration analysis of sandwich beams with honeycomb-corrugation hybrid cores. Compos Struct 171:335–344. https://doi.org/10.1016/j.compstruct.2017.03.045
21. Zhang Y, Li Y (2019) Nonlinear dynamic analysis of a double curvature honeycomb sandwich shell with simply supported boundaries by the homotopy analysis method. Compos Struct 221:110884. https://doi.org/10.1016/j.compstruct.2019.04.056
22. Keleshteri M, Asadi H, Aghdam M (2019) Nonlinear bending analysis of FG-CNTRC annular plates with variable thickness on elastic foundation. Thin-Walled Struct 135:453–462. https://doi.org/10.1016/j.tws.201[illegible].020
23. Ansari R, Torabi J (2019) Nonlinear free and forced vibration analysis of FG-CNTRC annular sector plates. Polym Compos 40(S2):E1[illegible]–E1377. https://doi.org/10.1002/pc.24998
24. Torabi J, Ansari R (2017) Nonlinear free vibration analysis of thermally induced FG-CNTRC annular plates: asymmetric versus axisymmetric study. Comput Methods Appl Mech Eng 324:327–347
25. Mou B, Li X, Bai Y, Wang L (2019) Shear behavior of panel zones in steel beam-to-column connections with unequal depth of outer annular stiffener. J Struct Eng 145(2):04018247
26. Mou B, Bai Y (2018) Experimental investigation on shear behavior of steel beam-to-CFST column connections with irregular panel zone. Eng Struct 168:487–504
27. Guo H, Li X, Zhu Q, Zhang Z, Liu Y, Li Z, Wen H, Li Y, Tang J, Liu J (2020) Imaging nano-defects of metal waveguides using the microwave cavity interference enhancement method. Nanotechnology 31(45):455203
28. Alam Z, Sun L, Zhang C, Su Z, Samali B (2020) Experimental and numerical investigation on the complex behaviour of the localised seismic response in a multi-storey plan-asymmetric structure. Struct Infrastruct Eng 1–17
29. Zhang C, Alam Z, Sun L, Su Z, Samali B (2019) Fibre Bragg grating sensor-based damage response monitoring of an asymmetric reinforced concrete shear wall structure subjected to progressive seismic loads. Struct Control Health Monit 26(3):e2307
30. Gholipour G, Zhang C, Mousavi AA (2020) Nonlinear numerical analysis and progressive damage assessment of a cable-stayed bridge pier subjected to ship collision. Mar Struct 69:102662
31. Kordestani H, Zhang C, Shadabfar M (2020) Beam damage detection under a moving load using random decrement technique and Savitzky-Golay Filter. Sensors 20(1):243
32. Mousavi AA, Zhang C, Masri SF, Gholipour G (2020) Structural Damage Localization and Quantification Based on a CEEMDAN Hilbert Transform Neural Network Approach: A Model Steel Truss Bridge Case Study. Sensors 20(5):1271
33. Li Z, Liu H, Dun Z, Ren L, Fang J (2020) Grouting effect on rock fracture using shear and seepage assessment. Constr Build Mater 242:118131
34. Al-Furjan MSH, Moghadam SA, Dehini R, Shan L, Habibi M, Safarpour H (2020) Vibration control of a smart shell reinforced by graphene nanoplatelets under external load: Semi-numerical and finite element modeling. Thin-Walled Struct. https://doi.org/10.1016/j.tws.2020.107242

35. Al-Furjan MSH, Dehini R, Paknahad M, Habibi M, Safarpour H (2021) On the nonlinear dynamics of the multi-scale hybrid nanocomposite-reinforced annular plate under hygro-thermal environment. Arch Civil Mech Eng 21(1):4. https://doi.org/10.1007/s43452-020-00151-w
36. Bousahla AA, Bourada F, Mahmoud S, Tounsi A, Algarni A, Bedia E, Tounsi A (2020) Buckling and dynamic behavior of the simply supported CNT-RC beams using an integral-first shear deformation theory. Comput Concrete 25 (2):155–166. https://doi.org/10.12989/cac.2020.25.2.155
37. Bourada F, Bousahla AA, Tounsi A, Bedia E, Mahmoud S, Benrahou KH, Tounsi A (2020) Stability and dynamic analyses of SW-CNT reinforced concrete beam resting on elastic-foundation. Comput Concrete 25 (6):485–495. https://doi.org/10.12989/cac.2020.25.6.485
38. Alimirzaei S, Mohammadimehr M, Tounsi A (2019) Nonlinear analysis of viscoelastic micro-composite beam with geometrical imperfection using FEM: MSGT electro-magneto-elastic bending, buckling and vibration solutions. Struct Eng Mech 71 (5):485–502. https://doi.org/10.12989/sem.2019.71.5.485
39. Bai Y, Alzahrani B, Baharom S, Habibi M (2020) Semi-numerical simulation for vibrational responses of the viscoelastic imperfect annular system with honeycomb core under residual pressure. Eng Comput 1–26
40. Wu H, Kitipornchai S, Yang J (2017) Imperfection sensitivity of thermal post-buckling behaviour of functionally graded carbon nanotube-reinforced composite beams. Appl Math Model 42:735–752. https://doi.org/10.1016/j.apm.2016.10.045
41. Zine A, Bousahla AA, Bourada F, Benrahou KH, Tounsi A, Adda Bedia E, Mahmoud S, Tounsi A (2020) Bending analysis of functionally graded porous plates via a refined shear deformation theory. Comput Concrete 26 (1):63–74. https://doi.org/10.12989/cac.2020.26.1.063
42. Kaddari M, Kaci A, Bousahla AA, Tounsi A, Bourada F, Tounsi A, Bedia E, Al-Osta MA (2020) A study on the structural behaviour of functionally graded porous plates on elastic foundation using a new quasi-3D model: Bending and free vibration analysis. Comput Concrete 25 (1):37–57. https://doi.org/10.12989/cac.2020.25.1.037
43. Addou FY, Meradjah M, Bousahla AA, Benachour A, Bourada F, Tounsi A, Mahmoud S (2019) Influence of porosity on dynamic response of FG plates resting on Winkler/Pasternak/Kerr foundation using quasi 3D HSDT. Comput Concrete 24(4):347–367
44. Berghouti H, Adda Bedia E, Benkhedda A, Tounsi A (2019) Vibration analysis of nonlocal porous nanobeams made of functionally graded material. Adv Nano Res 7 (5):351–364. https://doi.org/10.12989/anr.2019.7.5.351
45. Karimiasl M, Ebrahimi F, Mahesh V (2019) Nonlinear forced vibration of smart multiscale sandwich composite doubly curved porous shell. Thin-Walled Struct 143:106152
46. Al-Furjan M, Habibi M, Shan L, Tounsi A (2020) On the vibrations of the imperfect sandwich higher-order disk with a lactic core using generalize differential quadrature method. Compos Struct 113150
47. Gibson LJ, Ashby MF (1999) Cellular solids: structure and properties. Cambridge university press, Cambridge
48. Park J-S, Kim J-H, Moon S-H (2004) Vibration of thermally post-buckled composite plates embedded with shape memory alloy fibers. Compos Struct 63(2):179–188
49. Allam O, Draiche K, Bousahla AA, Bourada F, Tounsi A, Benrahou KH, Mahmoud S, Adda Bedia E, Tounsi A (2020) A generalized 4-unknown refined theory for bending and free vibration analysis of laminated composite and sandwich plates and shells. Comput Concrete 26 (2):185–201. https://doi.org/10.12989/cac.2020.26.2.185
50. Menasria A, Kaci A, Bousahla AA, Bourada F, Tounsi A, Benrahou KH, Tounsi A, Adda Bedia E, Mahmoud S (2020) A four-unknown refined plate theory for dynamic analysis of FG-sandwich plates under various boundary conditions. Steel Compos Struct 36(3):355–367
51. Rabhi M, Benrahou KH, Kaci A, Houari MSA, Bourada F, Bousahla AA, Tounsi A, Bedia EA, Mahmoud S, Tounsi A (2020) A new innovative 3-unknowns HSDT for buckling and free vibration of exponentially graded sandwich plates resting on elastic foundations under various boundary conditions. Geomech Eng 22 (2):119. https://doi.org/10.12989/gae.2020.22.2.119
52. Matouk H, Bousahla AA, Heireche H, Bourada F, Bedia E, Tounsi A, Mahmoud S, Tounsi A, Benrahou K (2020) Investigation on hygro-thermal vibration of P-FG and symmetric S-FG nanobeam using integral Timoshenko beam theory. Adv Nano Res 8(4):293–305
53. Chikr SC, Kaci A, Bousahla AA, Bourada F, Tounsi A, Bedia E, Mahmoud S, Benrahou KH, Tounsi A (2020) A novel four-unknown integral model for buckling response of FG sandwich plates resting on elastic foundations under various boundary conditions using Galerkin's approach. Geomech Eng 21(5):471–487. https://doi.org/10.12989/gae.2020.21.5.471
54. Refrafi S, Bousahla AA, Bouhadra A, Menasria A, Bourada F, Tounsi A, Bedia E, Mahmoud S, Benrahou KH, Tounsi A (2020) Effects of hygro-thermo-mechanical conditions on the buckling of FG sandwich plates resting on elastic foundations. Comput Concrete 25(4):311–325. https://doi.org/10.12989/cac.2020.25.4.311
55. Belbachir N, Bourada M, Draiche K, Tounsi A, Bourada F, Bousahla AA, Mahmoud S (2020) Thermal flexural analysis of anti-symmetric cross-ply laminated plates using a four variable refined theory. Smart Struct Syst 25 (4):409–422. https://doi.org/10.12989/sss.2020.25.4.409
56. Boutaleb S, Benrahou KH, Bakora A, Algarni A, Bousahla AA, Tounsi A, Tounsi A, Mahmoud S (2019) Dynamic analysis of nanosize FG rectangular plates based on simple nonlocal quasi 3D HSDT. Adv Nano Res 7(3):191. https://doi.org/10.12989/anr.2019.7.3.191
57. Reddy JN (2003) Mechanics of laminated composite plates and shells: theory and analysis. CRC press
58. Safarpour M, Ghabussi A, Ebrahimi F, Habibi M, Safarpour H (2020) Frequency characteristics of FG-GPLRC viscoelastic thick annular plate with the aid of GDQM. Thin-Walled Struct 150:106683
59. Ghabussi A, Habibi M, NoormohammadiArani O, Shavalipour A, Moayedi H, Safarpour H (2020) Frequency characteristics of a viscoelastic graphene nanoplatelet–reinforced composite circular microplate. J Vib Control 1077546320923930
60. Ghabussi A, Marnani JA, Rohanimanesh MS Improving seismic performance of portal frame structures with steel curved dampers. In: Structures, 2020. Elsevier, pp 27–40. https://doi.org/10.1016/j.istruc.2019.12.025
61. Ma X, Foong LK, Morasaei A, Ghabussi A, Lyu Z (2020) Swarm-based hybridizations of neural network for predicting the concrete strength. Smart Struct Syst 26(2):241–251
62. Al-Furjan M, Habibi M, Ghabussi A, Safarpour H, Safarpour M, Tounsi A (2020) Non-polynomial framework for stress and strain response of the FG-GPLRC disk using three-dimensional refined higher-order theory. Eng Struct 111496
63. Moayedi H, Darabi R, Ghabussi A, Habibi M, Foong LK (2020) Weld orientation effects on the formability of tailor welded thin steel sheets. Thin-Walled Struct 149:106669
64. Al-Furjan M, Habibi M, won Jung D, Safarpour H (2020) Vibrational characteristics of a higher-order laminated composite viscoelastic annular microplate via modified couple stress theory. Compos Struct 113152

65. Zhang C, Abedini M, Mehrmashhadi J (2020) Development of pressure-impulse models and residual capacity assessment of RC columns using high fidelity Arbitrary Lagrangian-Eulerian simulation. Eng Struct 224:111219
66. Alam Z, Zhang C, Samali B (2020) The role of viscoelastic damping on retrofitting seismic performance of asymmetric reinforced concrete structures. Earthq Eng Eng Vib 19(1):223–237
67. Sun L, Li C, Zhang C, Liang T, Zhao Z (2019) The strain transfer mechanism of fiber bragg grating sensor for extra large strain monitoring. Sensors 19(8):1851
68. Zheng J, Zhang C, Li A (2020) Experimental investigation on the mechanical properties of curved metallic plate dampers. Appl Sci 10(1):269
69. Gholipour G, Zhang C, Mousavi AA (2020) Numerical analysis of axially loaded RC columns subjected to the combination of impact and blast loads. Eng Struct 219:110924
70. SafarPour H, Hosseini M, Ghadiri M (2017) Influence of three-parameter viscoelastic medium on vibration behavior of a cylindrical nonhomogeneous microshell in thermal environment: An exact solution. J Therm Stress 40(11):1353–1367. https://doi.org/10.1080/01495739.2017.1350827
71. SafarPour H, Mohammadi K, Ghadiri M, Rajabpour A (2017) Influence of various temperature distributions on critical speed and vibrational characteristics of rotating cylindrical microshells with modified lengthscale parameter. Eur Phys J Plus 132(6):281
72. Al-Furjan M, Fereidouni M, Sedghiyan D, Habibi M, won Jung D (2020) Three-dimensional frequency response of the CNT-Carbon-Fiber reinforced laminated circular/annular plates under initially stresses. Compos Struct 113146
73. Al-Furjan M, Habibi M, Ebrahimi F, Mohammadi K, Safarpour H (2020) Wave dispersion characteristics of high-speed-rotating laminated nanocomposite cylindrical shells based on four continuum mechanics theories. Waves Random Complex Media 1–27
74. Al-Furjan M, Habibi M, Ebrahimi F, Chen G, Safarpour M, Safarpour H (2020) A coupled thermomechanics approach for frequency information of electrically composite microshell using heat-transfer continuum problem. Eur Phys J Plus 135(10):1–45
75. Hosseini-Hashemi S, Eshaghi M, Taher HRD (2010) An exact analytical solution for freely vibrating piezoelectric coupled circular/annular thick plates using Reddy plate theory. Compos Struct 92(6):1333–1351. https://doi.org/10.1016/j.compstruct.2009.11.006
76. Ghiasian S, Kiani Y, Sadighi M, Eslami M (2014) Thermal buckling of shear deformable temperature dependent circular/annular FGM plates. Int J Mech Sci 81:137–148. https://doi.org/10.1016/j.ijmecsci.2014.02.007
77. Khorasani M, Eyvazian A, Karbon M, Tounsi A, Lampani L, Sebaey TA (2020) Magneto-electro-elastic vibration analysis of modified couple stress-based three-layered micro rectangular plates exposed to multi-physical fields considering the flexoelectricity effects. Smart Struct Syst 26(3):331–343
78. Asghar S, Naeem MN, Hussain M, Taj M, Tounsi A (2020) Prediction and assessment of nonlocal natural frequencies of DWCNTs: Vibration analysis. Comput Concrete 25 (2):133–144. https://doi.org/10.12989/cac.2020.25.2.133
79. Gao N, Hou H, Zhang Y, Wu JH (2018) Sound absorption of a new oblique-section acoustic metamaterial with nested resonator. Mod Phys Lett B 32(04):1850040
80. Zhang C, Mousavi AA (2020) Blast loads induced responses of RC structural members: State-of-the-art review. Compos Part B Eng 108066
81. Li C, Sun L, Xu Z, Wu X, Liang T, Shi W (2020) Experimental investigation and error analysis of high precision FBG displacement sensor for structural health monitoring. Int J Struct Stability Dyn 2040011
82. Zhang C, Wang H (2020) Swing vibration control of suspended structures using the Active Rotary Inertia Driver system: theoretical modeling and experimental verification. Struct Control Health Monit 27(6):e2543
83. Zhang Z, Liu M, Zhou M, Chen J (2020) Dynamic reliability analysis of nonlinear structures using a Duffing-system-based equivalent nonlinear system method. Int J Approx Reason 126:84–97
84. Gao N, Wu JH, Yu L, Hou H (2016) Ultralow frequency acoustic bandgap and vibration energy recovery in tetragonal folding beam phononic crystal. Int J Mod Phys B 30(10):1650111
85. Huang Z, Zheng H, Guo L, Mo D (2020) Influence of the Position of Artificial Boundary on Computation Accuracy of Conjugated Infinite Element for a Finite Length Cylindrical Shell. Acoustics Aust 48(2):287–294
86. Zhang J, Chen Q, Sun J, Tian L, Zuo C (2020) On a universal solution to the transport-of-intensity equation. Opt Lett 45(13):3649–3652
87. Abedini M, Zhang C (2020) Performance Assessment of Concrete and Steel Material Models in LS-DYNA for Enhanced Numerical Simulation, A State of the Art Review. Arch Comput Methods Eng 1–22
88. Zhang C, Gholipour G, Mousavi AA (2020) State-of-the-Art Review on Responses of RC Structures Subjected to Lateral Impact Loads. Arch Comput Methods Eng 1–31
89. Zare R, Najaafi N, Habibi M, Ebrahimi F, Safarpour H (2020) Influence of imperfection on the smart control frequency characteristics of a cylindrical sensor-actuator GPLRC cylindrical shell using a proportional-derivative smart controller. Smart Struct Syst 26(4):469–480
90. Zhu L, Kong L, Zhang C (2020) Numerical study on hysteretic behaviour of horizontal-connection and energy-dissipation structures developed for prefabricated shear walls. Appl Sci 10(4):1240
91. Alam Z, Zhang C, Samali B (2020) Influence of seismic incident angle on response uncertainty and structural performance of tall asymmetric structure. The Structural Design of Tall and Special Buildings e1750
92. Abedini M, Mutalib AA, Zhang C, Mehrmashhadi J, Raman SN, Alipour R, Momeni T, Mussa MH (2020) Large deflection behavior effect in reinforced concrete columns exposed to extreme dynamic loads. Front Struct Civil Eng 14(2):532–553
93. Chen H, Zhang G, Fan D, Fang L, Huang L (2020) Nonlinear lamb wave analysis for microdefect identification in mechanical structural health assessment. Measurement 108026
94. Zhu Q (2019) Research on road traffic situation awareness system based on image big data. IEEE Intell Syst 35(1):18–26
95. Ni T, Liu D, Xu Q, Huang Z, Liang H, Yan A (2020) Architecture of cobweb-based redundant TSV for clustered faults. IEEE Trans Very Large Scale Integr (VLSI) Syst 28 (7):1736–1739
96. Ni T, Xu Q, Huang Z, Liang H, Yan A, Wen X (2020) A cost-effective TSV repair architecture for clustered faults in 3D IC. IEEE Trans Comput-Aided Design Integr Circuits Syst
97. Long Q, Wu C, Wang X (2015) A system of nonsmooth equations solver based upon subgradient method. Appl Math Comput 251:284–299
98. Zhu J, Wu P, Chen M, Kim MJ, Wang X, Fang T (2020) Automatically processing IFC clipping representation for BIM and GIS integration at the process level. Appl Sci 10 (6):2009
99. Wu C, Wang X, Chen M, Kim MJ (2019) Differential received signal strength based RFID positioning for construction equipment tracking. Adv Eng Inform 42:100960
100. Liu J, Wu C, Wu G, Wang X (2015) A novel differential search algorithm and applications for structure design. Appl Math Comput 268:246–269

101. Li T, Xu M, Zhu C, Yang R, Wang Z, Guan Z (2019) A deep learning approach for multi-frame in-loop filter of HEVC. IEEE Trans Image Process 28(11):5663–5678
102. Qian J, Feng S, Tao T, Hu Y, Li Y, Chen Q, Zuo C (2020) Deep-learning-enabled geometric constraints and phase unwrapping for single-shot absolute 3D shape measurement. APL Photon 5(4):046105
103. Tornabene F, Fantuzzi N, Ubertini F, Viola E (2015) Strong formulation finite element method based on differential quadrature: a survey. Appl Mech Rev 67 (2). https://doi.org/10.1115/1.4028859
104. Zhang C, Gholipour G, Mousavi AA (2019) Nonlinear dynamic behavior of simply-supported RC beams subjected to combined impact-blast loading. Eng Struct 181:124–142
105. Zhang C, Wang H (2019) Robustness of the active rotary inertia driver system for structural swing vibration control subjected to multi-type hazard excitations. Appl Sci 9(20):4391
106. Zhang C, Ou J (2015) Modeling and dynamical performance of the electromagnetic mass driver system for structural vibration control. Eng Struct 82:93–103
107. Mou B, Bai Y, Patel V (2020) Post-local buckling failure of slender and over-design circular CFT columns with high-strength materials. Eng Struct 210:110197
108. Safarpour M, Rahimi A, NoormohammadiArani O, Rabczuk T (2020) Frequency Characteristics of Multiscale Hybrid Nanocomposite Annular Plate Based on a Halpin-Tsai Homogenization Model with the Aid of GDQM. Appl Sci 10(4):1412
109. Karimiasl M, Ebrahimi F, Akgöz B (2019) Buckling and post-buckling responses of smart doubly curved composite shallow shells embedded in SMA fiber under hygro-thermal loading. Compos Struct 223:110988. https://doi.org/10.1016/j.compstruct.2019.110988

Publisher's Note Springer Nature remains neutral with regard to jurisdictional claims in published maps and institutional affiliations.